Experimental and Computational Multiphase Flow
Vol. 3, No. 1, 2021, 1–20
https://doi.org/10.1007/s42757-020-0061-7

Computational modeling of fiber transport in human respiratory airways—A review

Lin Tian[1] (✉), Goodarz Ahmadi[2]

1. School of Engineering – Mechanical and Automotive, RMIT University, Bundoora, VIC, Australia
2. Department of Mechanical and Aeronautical Engineering, Clarkson University, Potsdam, NY, USA

Abstract

Investigations on the respiratory transport and deposition of airborne asbestos, man-made vitreous fibers (MMVFs), and carbon nanofiber/carbon nanotubes have been actively conducted in the past few decades. The elongated particles' distinctive needle-like geometry has been identified as the main cause of extreme carcinogenicity when compared to inhaled spherical particles. Consequently, uncovering the intrinsic relationship between the particle's unique elongated shape and its transport characteristics in human respiratory systems is crucial for understanding fiber inhalation toxicity. Currently, such information can only be provided by computational modeling. This review summarized the current state of the art of computational modeling of fiber transport in the human respiratory tract. The needed future researches were also discussed.

Keywords

non-spherical particle
asbestos
fiber
computational modeling
transport and deposition
tracheobronchial tree
nasal cavity
respiratory airways

Article History

Received: 14 January 2020
Accepted: 14 February 2020

Review Article

1 Introduction

Occupational exposure to asbestos fibers or elongated mineral particles (EMPs) has been linked to the occurrence of malignant respiratory diseases such as mesothelioma and lung cancer (NIOSH, 2008). It is widely accepted that the respiratory pathological response to the inhaled asbestos fibers in humans and mammals is mainly induced by their deposition and retention in the airway. Measurements of particle deposition in human patient tissues as well as in vivo animal studies were reported by many researchers in the literature. Lippmann (1988), Pott et al. (1987), Wagner (1986), and NIOSH (1990) concluded that the mineral fiber dimension was the major determinant of their carcinogenicity, while the effect of the composition was negligible. EPA (2003) concluded that fibers with a length shorter than 5 μm posed a low risk, while the threshold for fiber diameter needed further investigation. NIOSH (2008) stated that fibers with a length smaller than 1.5 μm or greater than 40 μm with diameter thinner than 0.25 μm or thicker than 3 μm, respectively, had the highest risk to cause lung cancer.

As a substitute for asbestos in industrial and residential applications, man-made vitreous fibers (MMVFs) were considered non-carcinogenic under recommended exposure levels based on the epidemiological studies (Simonato et al., 1987; Marsh et al., 2001; IARC, 2002; Hesterberg et al., 2012; Lippmann, 2014). In addition, exposure to glass or mineral wool fibers (a subgroup to MMVFs) was neither found to be related to chest radiographic findings nor to change in lung functions (Hughes et al., 1993). However, potential inhalation hazards of MMVFs in high exposure conditions still raised increased concerns (Brown, 1994; Marsh et al., 2001; LeMasters et al., 2003; Cavallo et al., 2004; Nielsen and Koponen, 2018).

More recently, the rapid development of nanotechnology has seen increased usage of carbon nanotubes (CNTs) and carbon nanofiber (CNFs) (Invernizzi, 2011; Schubauer-Berigan et al., 2011). These nanofibers possess elongated cylindrical structures at micro/nano scales, resembling the appearance of asbestos. The analogy between the nanotubes/

✉ lin.tian@rmit.edu.au

nanofibers and asbestos and the similar biopersistence in the human body has raised concerns that the CNTs and CNFs could cause similar adverse pathologic responses in humans (Service, 1998). Though limited data is available for human assessment, animal studies have shown adverse pulmonary effects in rats and mice exposed to CNTs and CNFs (Lam et al., 2004; Poland et al., 2008; Porter et al., 2010; Murray et al., 2012). Adverse pulmonary responses, such as acute lung inflammation and interstitial fibrosis, were observed across various types of CNTs and CNFs in short-term and subchronic studies (Ma-Hock et al., 2009; Mercer et al., 2011). Longer and straighter CNTs tend to induce more asbestos-type mesothelial tumors than shorter ones (Poland et al., 2008; Murphy et al., 2011). When compared to other fibrogenic substances, including asbestos, the CNTs and CNFs are of similar or greater potency (Muller et al., 2005; Murray et al., 2012). It was also reported that agglomeration and formation of agglomerates affect the pulmonary response of animal subjects (Mercer et al., 2008; Porter et al., 2010; Murray et al., 2012). Though further long term animal study is needed to evaluate the carcinogenic potential of nanofibers, current findings confirmed the exposure risks of humans and animals to CNTs and CNFs.

In summary, airborne asbestos, human-made vitreous fibers (MMVFs), and carbon nanofiber/carbon nanotubes were observed or suspected to be highly carcinogenic, and the distinctive needle-like geometry was presumed to be the leading cause for carcinogenicity. Consequently, uncovering the intrinsic relationship between the particle's unique elongated shape and the pathological response in human respiratory airways is crucial for understanding the fiber inhalation toxicity. Some of the standing questions are:

- What are the correlations between the physical properties and the pathological responses?
- What are the mechanisms behind the correlations?
- Why longer fibers induce more asbestos-type mesothelial tumors than the shorter ones?
- How do the agglomeration and agglomerates change the behavior of the inhaled micron/nano-particles?

Answers to these questions will provide a better understanding of the phenomenon and a common ground for further scientific and industrial research to address the problem and for providing mitigation measures. For answering these questions, animal studies alone are not sufficient. In addition to the exposure input and the pathological outcome, the intermediate processes need to be revealed. This requires a close examination of the inhaled micron/nanofibers and their interactions with the pulmonary environment. With current technology, real-time physical examination of this nature on test subjects (in vitro/vivo) is impractical. The details of transport and deposition of micron/nanofibers can only be provided with simulations based on sound theoretical and computational models. Analyzing the fiber motion is a nontrivial task as the elongated particles cannot be simplified as a point sphere, and the rotational interactions induced by the geometric anisotropy needs to be resolved.

Dynamics of spherical particles have been extensively studied, and well-developed theories are available for analyzing particle motion in the entire Knudsen number range (Stokes, 1851; Einstein, 1905; Cunningham, 1910; Epstein, 1923; Saffman, 1965). On the contrary, such understanding is not fully available for non-spherical particles, where the theoretical expressions for the external forces (e.g., Stokes drag, lift, and Brownian) are profoundly affected by their irregular shapes. Theories on non-spherical particle dynamics are limited to a few regular shapes such as ellipsoids, cylinders, circular disks, and straight chain of agglomerated spheres (Oberbeck, 1876; Jeffery, 1922; Oseen, 1927; Burgers, 1938; Brenner, 1963; Batchelor, 1970). The motion and transport of irregular shaped particles were mainly investigated experimentally (McNown and Malaika, 1950; Horvath, 1974; Lasso and Weidmann, 1986; Cheng et al., 1988; Haider and Levenspiel, 1989; Chhabra et al., 1995; Cichocki and Hinsen, 1995; Tran-Cong et al., 2004). In addition to the challenge of resolving individual external forces, non-spherical particle dynamics requires the information on instantaneous particle orientation; therefore, the coupled translational and rotational momentum equations need to be solved simultaneously.

In current literature, the most elegant and cost-efficient methodology for evaluating the motion of dilute non-spherical particles is the Eulerian–Lagrangian (E–L) approach (or discrete phase modeling, DPM). In this approach, particles are considered a dispersed phase in the continuous flow, and their trajectories are individually examined. Attention to the individual particle rather than bulk approximation provides the means to extract detailed interaction between the particle and its environment. The approach also provides insights on correlating particle motion characteristics to its non-spherical geometry. Limitations of the E–L methodology are: (1) the restrictions of analytical expressions available to describe the external forces and torques applied to the non-spherical particle in the momentum equations; and (2) quality of the solution to Navier–Stokes equations for the continuous phase.

Using this approach, Fan and Ahmadi (1995a) investigated the wall deposition of ellipsoidal particles in turbulent flows using a sublayer model. By examining the fibrous particle trajectories, the effects of particle size, aspect ratio, particle to fluid density ratio, and gravity on particle deposition velocity were studied. Kvasnak and Ahmadi (1996) analyzed the deposition of ellipsoidal particles in a turbulent duct flow and accounted for the interactions between particle and turbulence fluctuations. By assembling the ellipsoidal fibers

into a rigid double link, Asgharian and Ahmadi (1998) developed a model of curved fiber using two ellipsoids connected at one end and investigated the effect of fiber geometry on their deposition in small lung airways. Fan et al. (1997) examined the flow-induced resuspension of rigid link fibers from surfaces.

Resolving the small particle molecular collision via a Brownian dynamics simulation, Fan and Ahmadi (2000) calculated the wall deposition of small ellipsoids from turbulent airflows. Employing flow solution from the direct numerical simulation (DNS), Zhang et al. (2001) studied the ellipsoidal particle transport and deposition in turbulent channel flows. Tian et al. (2012) reported the transport and deposition of ellipsoidal fibers in low Reynolds number pipe flow, where details of the fiber rotational motion were analyzed. Focusing on the fiber molecular diffusion, Tian et al. (2016, 2017) developed the semi-empirical governing equations for fiber diffusion and studied the isotropic and anisotropic diffusion properties of ellipsoidal fibers. In addition, they evaluated the orientational independent fiber equivalent spheres. Feng and Kleinstreuer (2013) analyzed the non-spherical particle transport in complex internal shear flows.

Using the E–L approach, Tavakol et al. (2017) extended the formulation of the governing equations to cover non-creeping hydrodynamic forces and torques for ellipsoidal inertial particles. Njobuenwu and Fairweather (2014, 2015, 2017) investigated the effect of shape on inertial particle dynamics in a channel flow for spherical, needle, and platelet-like particles using the large eddy simulations. Cui et al. (2018) reported a novel model for calculating the lift force acting on a prolate spheroidal particle in an arbitrary non-uniform flow. Li and Ma (2018) evaluated the deposition dynamics of rod-shaped colloids in porous media. By performing a large number of DNS simulations, Zastawny et al. (2012) derived the drag, lift, and torque coefficients for four different types of non-spherical particles (disk, fiber, and two ellipsoids) as a function of the Reynolds number, particle shape, and incidence angle between particle and the flow. Ouchene et al. (2016) performed a new set of correlations of drag, lift, and torque coefficients for non-spherical ellipsoidal particles at large Reynolds numbers. Yin et al. (2004) conducted numerical simulations of cylindrical particles in a burner model.

The presented literature survey clearly showed that the Eulerian–Lagrangian (E–L) approach was widely used for evaluating the non-spherical particle trajectories while accounting for the coupled translational and rotational motions. Also, all reported studies were concerned with regular-shaped particles (ellipsoids, spheroids, disks, and cylinders), where analytical expressions for the applied forces and torques are available. While researchers have continued to develop drags, lifts, and torques for other shaped particles (Hölzer and Sommerfeld, 2009; Guo et al., 2011; Zastawny et al., 2012; Luo et al, 2018), these developments are not complete to enable a full Eulerian–Lagrangian (E–L) modeling approach to suspension of particles of all shapes.

Assuming randomized orientation of the non-spherical particles, simplified Eulerian–Lagrangian (E–L) approach for analyzing the macroscale translational dynamics (rather than the instantaneous orientation of each particle) was reported in literature (Su and Cheng, 2005; Inthavong et al., 2008; Wang et al., 2008; Tian et al., 2016). Here an averaged drag coefficient accounting for the shape factors of all particles randomly oriented in the flow field was used. Stöber (1972) derived the dynamic shape factors of oblate and prolate ellipsoids based on the solution for fluid drag on ellipsoids (Oberbeck, 1876). Lasso and Weidman (1986) studied the Stokes drag on hollow cylinders and conglomerates of spheres. Haider and Levenspiel (1989) described the non-spherical particle drag coefficient correlation to its equivalent surface area. The empirical formulation of Tran-Cong et al. (2004) was proposed to describe an infinite set of irregularly shaped particles formed by the orderly arrangement of joined smaller spheres. All these studies provided orientation independent drag coefficient of non-spherical particles that can be used in the particle linear momentum equation.

The current review is focused on the conventional Eulerian–Lagrangian (E–L) approach for analyzing non-spherical particle transport and deposition in human respiratory airways. The gas flow is typically evaluated using the Reynolds averaged Navier–Stokes (RANS) equations. The more computationally intensive DNS and immersed boundary method (IBM), as well as the DNS-fictitious domain method (FDM) for suspension of non-spherical particles in gas flows, are outside the scope of the current review.

2 Eulerian–Lagrangian (E–L) methodology

In the Eulerian–Lagrangian (E–L) approach, particles are considered the dispersed phase in the continuous flow and individually examined. For dilute suspension considered in this review, the presence of particles does not affect the flow field. The continuous flow field is governed by the Navier–Stokes (or RANS) equations and solved in the Eulerian framework. The dispersed phase, including the spherical or non-spherical particles, is governed by Newton's second law. The solution is achieved after resolving all dynamic interactions between the particle and its external environment. Particle trajectories can be evaluated by integrating the governing equation in the Lagrangian framework. Solutions to the continuous flow field are decoupled from the dispersed particle phase, while particles are carried by the gas flow under that assumption of one-way coupling.

The Eulerian–Lagrangian (E–L) method is flexible in

handling the continuous flow phase by using a variety of solution strategies (e.g., laminar, turbulence models, DNS, and LES). While the non-spherical particle motions can be evaluated through the proper formulation of the gas flow environment on the particle. In this section, the theories, methodologies, and computational procedures for non-spherical fiber particles in the Lagrangian frame are described in detail, followed by a brief discussion of the continuous flow phase simulation.

2.1 Kinematics of fiber particle

Figure 1 shows the coordinate systems associated with the motion of an ellipsoidal particle in a general flow field. Here, $\boldsymbol{x} = [x, y, z]$ is the inertial coordinate, and $\hat{\boldsymbol{x}} = [\hat{x}, \hat{y}, \hat{z}]$ is the particle coordinate system with its origin being at the particle mass center and its axes being the principal axes. In this figure, a third coordinate system $\hat{\hat{\boldsymbol{x}}} = [\hat{\hat{x}}, \hat{\hat{y}}, \hat{\hat{z}}]$ with its origin coinciding with that of the particle frame and its axes being parallel to the corresponding axes of the inertial frame is also shown. This third coordinate system will be referred to as the co-moving frame. The transformation between the co-moving frame coordinates and the particle frame coordinates is given by the linear relation:

$$\hat{\boldsymbol{x}} = \boldsymbol{A}\hat{\hat{\boldsymbol{x}}} \tag{1}$$

Here the transformation matrix $\boldsymbol{A} = [a_{ij}]$ may be expressed in terms of Euler angles or Euler's four parameters (quaternions) (Goldstein, 1980; Hughes, 1986), i.e.,

$$\boldsymbol{A} = \begin{bmatrix} \cos\varphi\cos\phi - \cos\theta\sin\phi\sin\varphi & \cos\varphi\sin\phi + \cos\theta\cos\phi\sin\varphi & \sin\varphi\sin\theta \\ -\sin\varphi\cos\phi - \cos\theta\sin\phi\cos\varphi & -\sin\varphi\sin\phi + \cos\theta\cos\phi\cos\varphi & \cos\varphi\sin\theta \\ \sin\theta\sin\phi & -\sin\theta\cos\phi & \cos\theta \end{bmatrix} \tag{2}$$

or

$$\boldsymbol{A} = \begin{bmatrix} 1-2(\varepsilon_2^2+\varepsilon_3^2) & 2(\varepsilon_1\varepsilon_2+\varepsilon_3\eta) & 2(\varepsilon_1\varepsilon_3-\varepsilon_2\eta) \\ 2(\varepsilon_2\varepsilon_1-\varepsilon_3\eta) & 1-2(\varepsilon_3^2+\varepsilon_1^2) & 2(\varepsilon_2\varepsilon_3+\varepsilon_1\eta) \\ 2(\varepsilon_3\varepsilon_1+\varepsilon_2\eta) & 2(\varepsilon_3\varepsilon_2-\varepsilon_1\eta) & 1-2(\varepsilon_1^2+\varepsilon_2^2) \end{bmatrix} \tag{3}$$

Here ϕ, θ, and φ are Euler angles (the x-convention of Goldstein (1980)), while ε_1, ε_2, ε_3, η are Euler's four parameters. Figure 2 illustrates the definitions of Euler angles and Euler's four parameters. The Euler's parameters are related to the axis and angle of rotation by $(\varepsilon_1, \varepsilon_2, \varepsilon_3)^{\mathrm{T}} = \boldsymbol{e}\sin(\Omega/2)$ and $\eta = \cos(\Omega/2)$, where a superscript T denotes a transpose. Due to the inevitable singularity in evaluating the time rates of changes of Euler angles (Fan and Ahmadi, 1995b), Eq. (3)

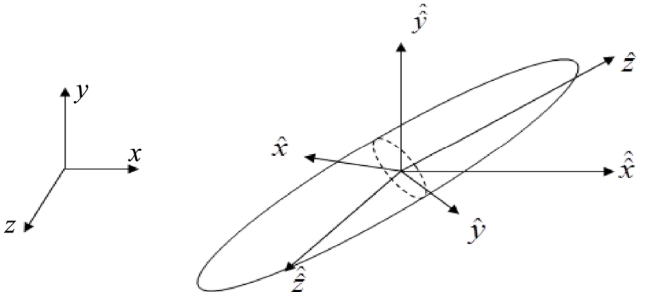

Fig. 1 An ellipsoidal fiber particle and the corresponding coordinate systems (Tian and Ahmadi, 2016a; reproduced with permission © ASME 2016).

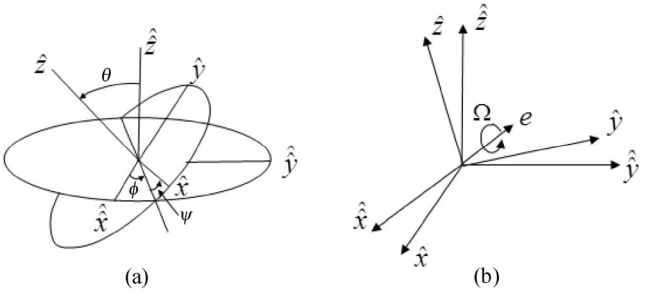

Fig. 2 Linear transformation of coordinate systems: (a) Euler angles; (b) Euler's quaternions (Tian and Ahmadi, 2016a; reproduced with permission © ASME 2016).

is used in the numerical simulation of particle motions. However, Euler angles, which are mutually independent variables and Eq. (2), are used to assign the initial particle orientations.

The most general rotation of a rigid body has three degrees of freedom. Therefore, Euler's four parameters are subject to a constraint given by

$$\varepsilon_1^2 + \varepsilon_2^2 + \varepsilon_3^2 + \eta^2 = 1 \tag{4}$$

The four parameters may also be expressed in terms of the elements of the transformation matrix. That is, for $\eta \neq 0$,

$$\eta = \pm\frac{1}{2}(1 + a_{11} + a_{11} + a_{11})^{1/2} \tag{5}$$

$$\begin{bmatrix} \varepsilon_1 \\ \varepsilon_2 \\ \varepsilon_3 \end{bmatrix} = \frac{1}{4\eta}\begin{bmatrix} a_{23} - a_{32} \\ a_{31} - a_{13} \\ a_{12} - a_{21} \end{bmatrix} \tag{6}$$

For $\eta = 0$,

$$\varepsilon_1 = \pm\sqrt{\frac{1 + a_{11}}{2}} \tag{7}$$

$$\varepsilon_2 = \frac{a_{12}}{2\varepsilon_1} \tag{8}$$

$$\varepsilon_3 = \frac{a_{23}}{2\varepsilon_2} \tag{9}$$

where a_{ij} (elements of $\boldsymbol{A}$) are the direction cosines. The time rates of change of the Euler quaternion (ε_1, ε_2, ε_3, η) are related to the fiber angular velocities ($\omega_{\hat{x}}$, $\omega_{\hat{y}}$, $\omega_{\hat{z}}$) in the particle frame. That is,

$$\begin{bmatrix} \frac{d\varepsilon_1}{dt} \\ \frac{d\varepsilon_2}{dt} \\ \frac{d\varepsilon_3}{dt} \\ \frac{d\eta}{dt} \end{bmatrix} = \frac{1}{2} \begin{bmatrix} \eta\omega_{\hat{x}} - \varepsilon_3\omega_{\hat{y}} + \varepsilon_2\omega_{\hat{z}} \\ \varepsilon_3\omega_{\hat{x}} + \eta\omega_{\hat{y}} - \varepsilon_1\omega_{\hat{z}} \\ -\varepsilon_2\omega_{\hat{x}} + \varepsilon_1\omega_{\hat{y}} + \eta\omega_{\hat{z}} \\ -\varepsilon_1\omega_{\hat{x}} - \varepsilon_2\omega_{\hat{y}} - \varepsilon_3\omega_{\hat{z}} \end{bmatrix} \tag{10}$$

Here t is the time. The translational displacement of the particle is described by

$$\frac{d\boldsymbol{x}}{dt} = \boldsymbol{v} \tag{11}$$

here $\boldsymbol{v}$ is the translational velocity vector of the particle mass center in the inertial coordinate.

2.2 Dynamics of fiber particle

For a non-spherical particle moving in a general flow field, the translational and the rotational motions are governed by

$$m^p \frac{d\boldsymbol{v}}{dt} = m^p \boldsymbol{g} + \boldsymbol{f}^h + \boldsymbol{f}^L + \boldsymbol{f}^B(t) \tag{12}$$

$$I_{\hat{x}} \frac{d\omega_{\hat{x}}}{dt} - \omega_{\hat{y}}\omega_{\hat{z}}(I_{\hat{y}} - I_{\hat{z}}) = T_{\hat{x}}^h + T_{\hat{x}}^B(t) \tag{13}$$

$$I_{\hat{y}} \frac{d\omega_{\hat{y}}}{dt} - \omega_{\hat{z}}\omega_{\hat{x}}(I_{\hat{z}} - I_{\hat{x}}) = T_{\hat{y}}^h + T_{\hat{y}}^B(t) \tag{14}$$

$$I_{\hat{z}} \frac{d\omega_{\hat{z}}}{dt} - \omega_{\hat{x}}\omega_{\hat{y}}(I_{\hat{x}} - I_{\hat{y}}) = T_{\hat{z}}^h + T_{\hat{z}}^B(t) \tag{15}$$

In the above equations, $\boldsymbol{v}$ is the centroidal translational velocity, and ($\omega_{\hat{x}}$,$\omega_{\hat{y}}$,$\omega_{\hat{z}}$) is the components of the angular velocity vector. Here, m^p is the mass of the fiber, $\boldsymbol{g}$ is the gravitational acceleration, $\boldsymbol{f}^h$ is the hydrodynamic drag, $\boldsymbol{f}^L$ is the shear-induced lift force, and $\boldsymbol{f}^B$ is the Brownian diffusion force. In Eqs. (13)–(15), ($I_{\hat{x}}$, $I_{\hat{y}}$, $I_{\hat{z}}$) is the moment of inertia about the principle axes in the particle frame, and ($T_{\hat{x}}^h$,$T_{\hat{y}}^h$,$T_{\hat{z}}^h$) and ($T_{\hat{x}}^B$,$T_{\hat{y}}^B$,$T_{\hat{z}}^B$) are, respectively, the hydrodynamic and Brownian torques acted on the fiber. It is noted that the governing equations (12)–(15) are general and apply to all irregular shaped particles.

2.3 Interactions of the fiber particle with external environment

Solutions to the fiber equations of motion (12)–(15) require the resolution of interactive forces between the fiber and environmental, which appear on the right-hand side of the governing equations. Formulations of each individual term on the various forces and torques are in general shape dependent.

2.3.1 *Hydrodynamic drag*

The hydrodynamic drag force acting on an arbitrary shaped particle in a general flow field under the Stokes flow regime was obtained by Brenner (1963) in the form of an infinite series of fluid velocity and its spatial derivatives. The higher-order terms are proportional to higher-order powers of particle minor axis. Retaining only the first term of the series for small particles, it follows that

$$\boldsymbol{f}^h = \mu\pi a\hat{\hat{\boldsymbol{K}}} \cdot (\boldsymbol{u} - \boldsymbol{v}) \tag{16}$$

where μ is the fluid viscosity, a is the semi-minor axis of the ellipsoid of revolution, and $\boldsymbol{u}$ is the fluid velocity vector at the fiber centroid. In Eq. (16), $\hat{\hat{\boldsymbol{K}}}$ is the translational dyadic in the co-moving frame given by

$$\hat{\hat{\boldsymbol{K}}} = \boldsymbol{A}^{-1}\hat{\boldsymbol{K}}\boldsymbol{A} \tag{17}$$

The translational dyadic $\hat{\boldsymbol{K}}$ in the fiber frame is a diagonal matrix. For an ellipsoid of revolution along the $\hat{z}$-axis, the diagonal elements are (Jeffery, 1922; Oseen, 1927):

$$K_{\hat{x}\hat{x}} = K_{\hat{y}\hat{y}} = \frac{16(\beta^2 - 1)}{C_{\hat{x}}^t\{[(2\beta^2 - 3)\ln(\beta + \sqrt{\beta^2 - 1}) / \sqrt{\beta^2 - 1}] + \beta\}} \tag{18}$$

$$K_{\hat{z}\hat{z}} = \frac{8(\beta^2 - 1)}{C_{\hat{z}}^t\{[(2\beta^2 - 1)\ln(\beta + \sqrt{\beta^2 - 1}) / \sqrt{\beta^2 - 1}] - \beta\}} \tag{19}$$

Here β is the aspect ratio defined as the ratio of fiber's length over its diameter. C_i^t s are the translational slip-correction factors (Fan and Ahmadi, 2000). It is noted that C_i^t is only significant in high Knudsen number flows and reduces to identify for inertial particles. Details of C_i^t is given in subsequent sections.

2.3.2 *Shear-induced lift*

The shear-induced lift force acting on an arbitrary-shaped particle was obtained by Harper and Chang (1968). For an ellipsoid of revolution in a simple shear flow, the lift force, due to the dominant streamwise flow shear, can be expressed as

$$\boldsymbol{f}^L = \frac{\pi^2\mu a^2}{\nu^{\frac{1}{2}}} \frac{\frac{\partial u_x}{\partial y}}{\left|\frac{\partial u_x}{\partial y}\right|^{\frac{1}{2}}} (\hat{\hat{\boldsymbol{K}}} \cdot \boldsymbol{L} \cdot \hat{\hat{\boldsymbol{K}}}) \cdot (\boldsymbol{u}^L - \boldsymbol{v}) \tag{20}$$

here $\boldsymbol{u}^L = (u_x, 0, 0)$ is the reference flow for the lift, and

$$\boldsymbol{L} = \begin{vmatrix} 0.0501 & 0.0329 & 0.00 \\ 0.0182 & 0.0173 & 0.00 \\ 0.00 & 0.00 & 0.0373 \end{vmatrix} \tag{21}$$

is the lift tensor.

2.3.4 Brownian diffusion force

The Brownian diffusion force $\boldsymbol{f}^{\boldsymbol{B}}$ in the inertial frame is given as

$$\boldsymbol{f}^{\boldsymbol{B}} = \hat{\hat{\boldsymbol{f}}}^{\boldsymbol{B}} = \boldsymbol{A}^{-1}\hat{\boldsymbol{f}}^{\boldsymbol{B}} \tag{22}$$

here $\hat{\boldsymbol{f}}^{\boldsymbol{B}} = [f_{\hat{x}}^B, f_{\hat{y}}^B, f_{\hat{z}}^B]$] is the Brownian force expressed in the particle coordinate. The component of Brownian forces can be modeled as independent zero-mean Gaussian white-noise processes with the following statistics (Uhlenbeck and Ornstein, 1930; Chandrasekhar, 1943; Gupta and Peters, 1985; Ounis et al., 1991):

$$< \hat{\boldsymbol{f}}^{\boldsymbol{B}}(t) >= 0, \ < \hat{\boldsymbol{f}}^{\boldsymbol{B}}(t) \otimes \hat{\boldsymbol{f}}^{\boldsymbol{B}}(t+t') >= \pi \boldsymbol{S}^{\boldsymbol{t}} \delta(t') \tag{23}$$

Here t' is the time lag, $\delta(\ )$ is the Dirac delta function, a pair of angular brackets < > stands for the ensemble average, and the correlations are obtained by averaging the time-shifted dyadic products. In the above equations, $\boldsymbol{S}^{\boldsymbol{t}}$ is the spectral intensity tensors for the translational Brownian motion, which is a diagonal matrix in the fiber frame. That is

$$S_{\hat{i}\hat{i}}^t = 2\kappa\vartheta R_{\hat{i}\hat{i}}^t / \pi \tag{24}$$

Here κ is the Boltzmann constant, ϑ is the absolute temperature, and $R_{\hat{i}\hat{i}}^t$ is the resistant coefficients for an ellipsoidal translating along its principal axes in a quiescent fluid, which are given by

$$R_{\hat{x}\hat{x}}^t = \pi\mu a K_{\hat{x}\hat{x}}, \ R_{\hat{y}\hat{y}}^t = \pi\mu a K_{\hat{y}\hat{y}}, \ R_{\hat{z}\hat{z}}^t = \pi\mu a K_{\hat{z}\hat{z}} \tag{25}$$

2.3.5 Hydrodynamic torque

The hydrodynamic torque acting on an ellipsoidal fiber suspended in a linear shear flow is given by Jeffrey (1922). Accordingly, for an ellipsoid of revolution with its major axis along the $\hat{z}$-axis, the hydrodynamic torques are given by

$$T_{\hat{x}}^h = \frac{16\pi\mu a^3\beta}{3(\beta_0 + \beta^2\gamma_0)C_{\hat{x}}^r}\left[(1-\beta^2)d_{\hat{z}\hat{y}} + (1+\beta^2)(w_{\hat{z}\hat{y}} - \omega_{\hat{x}})\right] \tag{26}$$

$$T_{\hat{y}}^h = \frac{16\pi\mu a^3\beta}{3(\alpha_0 + \beta^2\gamma_0)C_{\hat{y}}^r}\left[(\beta^2-1)d_{\hat{x}\hat{z}} + (1+\beta^2)(w_{\hat{x}\hat{z}} - \omega_{\hat{y}})\right] \tag{27}$$

$$T_{\hat{z}}^h = \frac{32\pi\mu a^3\beta}{3(\alpha_0 + \beta_0)C_{\hat{z}}^r}(w_{\hat{y}\hat{x}} - \omega_{\hat{z}}) \tag{28}$$

Here

$$d_{\hat{z}\hat{y}} = \frac{1}{2}\left(\frac{\partial u_{\hat{z}}}{\partial \hat{y}} + \frac{\partial u_{\hat{y}}}{\partial \hat{z}}\right), \ d_{\hat{x}\hat{z}} = \frac{1}{2}\left(\frac{\partial u_{\hat{x}}}{\partial \hat{z}} + \frac{\partial u_{\hat{z}}}{\partial \hat{x}}\right) \tag{29}$$

$$w_{\hat{z}\hat{y}} = \frac{1}{2}\left(\frac{\partial u_{\hat{z}}}{\partial \hat{y}} - \frac{\partial u_{\hat{y}}}{\partial \hat{z}}\right), \ w_{\hat{x}\hat{z}} = \frac{1}{2}\left(\frac{\partial u_{\hat{x}}}{\partial \hat{z}} - \frac{\partial u_{\hat{z}}}{\partial \hat{x}}\right),$$
$$w_{\hat{y}\hat{x}} = \frac{1}{2}\left(\frac{\partial u_{\hat{y}}}{\partial \hat{x}} - \frac{\partial u_{\hat{x}}}{\partial \hat{y}}\right) \tag{30}$$

Equations (26)–(28) assume that the flow near a small particle may locally be approximated as a linear shear flow at low Reynolds numbers. C_i^r s in Eqs. (26)–(28) are the rotational slip-correction factors (Fan and Ahmadi, 2000). Similar to the translational C_i^t, the rotational C_i^r is only significant for high-Knudsen number flows (submicron particles) and reduces to identity for inertial fibers. The expression for C_i^r is given in the subsequent section. Equations (29) and (30) are, respectively, the fluid deformation rate tensor and the spin tensor. In principle, the velocities in these equations are the instantaneous velocities including the turbulent fluctuations. In the viscous sublayer, the turbulence fluctuations are negligible and in the evaluation of the hydrodynamic torques given by Eqs. (26)–(28), the gradient of velocity fluctuation is neglected. The dimensionless parameters in Eqs. (26)–(28) are given by Gallily and Cohen (1979) as

$$\alpha_0 = \beta_0 = \frac{\beta^2}{\beta^2-1} + \frac{\beta}{2(\beta^2-1)^{\frac{3}{2}}}\ln\left(\frac{\beta - \sqrt{\beta^2-1}}{\beta + \sqrt{\beta^2-1}}\right) \tag{31}$$

$$\gamma_0 = -\frac{2}{\beta^2-1} - \frac{\beta}{(\beta^2-1)^{\frac{3}{2}}}\ln\left(\frac{\beta - \sqrt{\beta^2-1}}{\beta + \sqrt{\beta^2-1}}\right) \tag{32}$$

The velocity gradient in Eqs. (29) and (30) can be obtained by using the following transformation:

$$\hat{\boldsymbol{G}} = \boldsymbol{A}\hat{\hat{\boldsymbol{G}}}\boldsymbol{A}^{-1} \tag{33}$$

where $\hat{\boldsymbol{G}}$ and $\hat{\hat{\boldsymbol{G}}}$ stand for the dyadic, respectively, expressed in the fiber and the co-moving frames.

2.3.6 Brownian diffusion torque

The Brownian diffusion torque in the particle frame can be modeled as independent zero-mean Gaussian white-noise processes in the following form (Uhlenbeck and Ornstein, 1930; Chandrasekhar, 1943; Gupta and Peters, 1985; Ounis et al., 1991):

$$< \hat{T}^B(t) >= 0, \ < \hat{T}^B(t) \otimes \hat{T}^B(t+t') >= \pi \boldsymbol{S}^{\boldsymbol{r}} \delta(t') \tag{34}$$

Here $\boldsymbol{S}^{\boldsymbol{r}}$ is the spectral intensity tensors for the rotational Brownian motion, which is a diagonal matrix in the fiber frame, and is given as

$$S_{ii}^r = 2\kappa\vartheta R_{ii}^r / \pi \tag{35}$$

In the above expression, R_{ii}^r are the resistance coefficients for an ellipsoid rotating about its principal axes in a quiescent fluid:

$$R_{\hat{x}\hat{x}}^r = \frac{16\pi\mu a^2}{3}K_{\hat{x}}^r,\quad R_{\hat{y}\hat{y}}^r = \frac{16\pi\mu a^2}{3}K_{\hat{y}}^r,\quad R_{\hat{z}\hat{z}}^r = \frac{16\pi\mu a^2}{3}K_{\hat{z}}^r \tag{36}$$

where

$$K_{\hat{x}}^r = \frac{a\beta(1+\beta^2)}{(\beta_0+\beta^2\gamma_0)C_{\hat{x}}^r},\quad K_{\hat{y}}^r = \frac{a\beta(1+\beta^2)}{(\alpha_0+\beta^2\gamma_0)C_{\hat{y}}^r},$$
$$K_{\hat{z}}^r = \frac{a\beta}{(\alpha_0+\beta_0)C_{\hat{z}}^r} \tag{37}$$

2.3.7 Fiber mass and moments of inertia

The mass of an ellipsoidal fiber is

$$m^p = \frac{4}{3}\pi a^3\beta\rho^p \tag{38}$$

where ρ^p is the particle density. The principal moments of inertia for the fiber particle are

$$I_{\hat{x}} = I_{\hat{y}} = \frac{(1+\beta^2)a^2}{5}m^p,\quad I_{\hat{z}} = \frac{2a^2}{5}m^p \tag{39}$$

2.4 Fiber slip correction

In the free molecular regime where the characteristic length scale of the fiber is smaller than the gas mean free path, the hydrodynamic drag and torque, developed under the assumption of a continuum regime, need to be modified. The slip corrections for the translation and rotation of an ellipsoidal fiber in Eqs. (18), (19), (26)–(28), and (37) are derived based on the procedures suggested by Dahneke (1973). The derived slip correction factors are applicable to the free molecular regime, the transition regime, and the continuum regime where the correction factors are reduced to identity.

2.4.1 Translational slip correction

Using statistical mechanics, Dahneke (1973) obtained the translational tensor components for ellipsoidal particles in the free molecular regime, which is

$$K_{\hat{x}\hat{x}} = K_{\hat{y}\hat{y}} = \frac{\beta}{Kn}\left\{E_p\left[4+\left(\frac{\pi}{2}-1\right)\alpha\right]+\frac{G_p}{F_p^2}\left(2+\frac{4F_p^2+\pi-6}{4}\right)\alpha\right\} \tag{40}$$

$$K_{\hat{z}\hat{z}} = \frac{\beta}{Kn}\left\{2E_p\alpha+\frac{G_p}{F_p^2}\left[F_p^2(4-2\alpha)-4+\left(3-\frac{\pi}{2\beta^2}\right)\alpha\right]\right\} \tag{41}$$

where

$$E_p = \frac{\sin^{-1}F_p}{F_p},\quad F_p = \sqrt{1-\frac{1}{\beta^2}},\quad G_p = \frac{1}{\beta}-E_p \tag{42}$$

In Eqs. (40)–(42), $Kn = \lambda/a$ is the Knudsen number, λ is the mean free path of the fluid, and α is the particle momentum accommodation coefficient. Based on Eqs. (18), (19) and (40), (41), the free molecular slip correction factors are obtained as

$$C_{\hat{x}}^t|_{fm} = C_{\hat{y}}^t|_{fm} = \frac{16(\beta^2-1)Kn}{\beta(B\cdot C)},\quad C_{\hat{z}}^t|_{fm} = \frac{8(\beta^2-1)Kn}{\beta(D\cdot E)} \tag{43}$$

$$B = \frac{2\beta^2-3}{\sqrt{\beta^2-1}}\ln\left(\beta+\sqrt{\beta^2-1}\right)+\beta \tag{44}$$

$$C = E_p\left[4+\left(\frac{\pi}{2}-1\right)\alpha\right]+\frac{G_p}{F_p^2}\left(2+\frac{4F_p^2+\pi-6}{4}\right)\alpha \tag{45}$$

$$D = \frac{2\beta^2-1}{\sqrt{\beta^2-1}}\ln\left(\beta+\sqrt{\beta^2-1}\right)-\beta \tag{46}$$

$$E = 2E_p\alpha+\frac{G_p}{F_p^2}\left[F_p^2(4-2\alpha)-4+\left(3-\frac{\pi}{2\beta^2}\right)\alpha\right] \tag{47}$$

The translational slip correction factors of ellipsoidal fiber, covering all flow regimes, can be obtained by ensuring a smooth transition from the free molecular regime to the continuum regime. These are

$$C_{\hat{x}}^t = C_{\hat{y}}^t = 1+\frac{a}{r_{\hat{x}}^t}Kn\left[1.257+0.4\exp\left(\frac{-1.1r_{\hat{x}}^t}{aKn}\right)\right] \tag{48}$$

$$C_{\hat{z}}^t = 1+\frac{a}{r_{\hat{z}}^t}Kn\left[1.257+0.4\exp\left(\frac{-1.1r_{\hat{z}}^t}{aKn}\right)\right] \tag{49}$$

where

$$r_{\hat{x}}^t = \frac{1.657a\beta}{16(\beta^2-1)}(B\cdot C),\quad r_{\hat{z}}^t = \frac{1.657a\beta}{8(\beta^2-1)}(D\cdot E) \tag{50}$$

2.4.2 Rotational slip correction

Accurate expressions for the rotational slip-correction factors of an ellipsoidal fiber are not available due to the lack of theoretical studies and experimental data. For ellipsoids with high aspect ratios ($\beta >> 1$), the rotational slip-correction is approximated as that of a cylindrical particle following similar procedures to derive the translational slip correction (Fan and Ahmadi, 2000). In the continuum regime, the

rotational resistance tensor is given by Gans (1928) as

$$f_{\hat{x}}^r = f_{\hat{y}}^r = \frac{(6\pi/3)\mu a^3\beta^3}{\ln(2\beta)+0.1931} \tag{51}$$

and in the free molecular regime, the rotational resistance tensor is given by Eisner and Gallily (1981) as

$$f_{\hat{x}}^r = f_{\hat{y}}^r = \frac{8\pi\mu^3 a^3\beta^3}{Kn}\left[\left(\frac{1}{4}+\frac{1}{4\beta}+\frac{1}{4\beta^2}+\frac{1}{8\beta^3}\right) + \alpha\left(\frac{\pi-6}{48}-\frac{1}{8\beta}-\frac{1}{8\beta^2}+\frac{\pi-4}{64\beta^3}\right)\right] \tag{52}$$

Universal equations for the rotational slip correction factors of the ellipsoidal fiber, covering all flow regimes, can be obtained by ensuring a smooth transition from the free molecular regime to the continuum regime. That is

$$C_{\hat{x}}^r = C_{\hat{y}}^r = 1+\frac{a}{r_{\hat{x}}^r}Kn\left[1.257+0.4\exp\left(\frac{-1.1r_{\hat{x}}^r}{aKn}\right)\right] \tag{53}$$

Here

$$r_{\hat{x}}^r = \frac{4.971a}{8}[\ln(2\beta)+0.1931]\left[\left(\frac{1}{4}+\frac{1}{4\beta}+\frac{1}{4\beta^2}+\frac{1}{8\beta^3}\right) + \alpha\left(\frac{\pi-6}{48}-\frac{1}{8\beta}-\frac{1}{8\beta^2}+\frac{\pi-4}{64\beta^3}\right)\right] \tag{54}$$

The rotational slip correction in the $\hat{z}$-direction is neglected as the rotation in the $\hat{z}$-direction is expected to have minimum effect toward the fiber translation and deposition.

2.5 Computational modeling procedures

2.5.1 *Computational algorithm*

The computational algorithms for solving the translation and rotation of an ellipsoidal fiber in a 3D flow field are:

1. Initialize the ellipsoidal fiber particle's position, orientation, velocity, and angular velocity.
2. Compute fiber orientation by using Euler's quaternion (Eq. (2) or (3)).
3. Solve Eqs. (12)–(15) simultaneously at each time step and evaluate:
   a. Hydrodynamic drag by using Eq. (16).
   b. Shear-induced lift by using Eq. (20).
   c. Brownian diffusion force by using Eqs. (22) and (23).
   d. Hydrodynamic torque by using Eqs. (26)–(28).
   e. Brownian diffusion torque by using Eq. (34).
   f. Flow phase velocity and shear gradient by using Eqs. (29) and (30).
4. Update fiber particle's position.
5. Update fiber particle's Euler quaternion by using Eq. (10).
6. Go back to step 2 and repeat the computation until the termination condition is met. That is
   a. The fiber particle is deposited.
   b. The fiber particle goes out of the domain.
   c. The maximum computation time step is reached.

2.5.2 *Boundary condition—fiber deposition on a smooth surface*

When the ellipsoidal fiber particle comes into contact with the wall boundary, it is deposited due to the adhesion force. The deposition of an ellipsoidal fiber is a function of its mass of center position and its orientation relative to the wall. Three deposition scenarios could occur: (1) if the distance of the fiber's center of mass from the boundary surface is smaller than the semi-minor axis, it will be deposited; (2) if this relative position is greater than the semi-major axis, the fiber will not be trapped; (3) when the distance between the fiber's mass center and the wall boundary is within the range of its semi-minor and semi-major axes, whether the fiber is deposited or not depends on its orientation relative to the wall.

Figure 3 shows the deposition of an ellipsoidal fiber in scenario three, where the coordinate is described locally in the particle and the co-moving frame. If the unit vector (0, 0, 1) is attached to the fiber's major principle axis in the particle frame, the projection of this unit vector onto the local co-moving frame is given by

$$l = \sqrt{a_{31}^2 + a_{33}^2} \tag{55}$$

Here a_{31} and a_{33} are from the Euler's quaternion as shown in Eq. (3). The inclination angle between the particle's principal axis in the particle frame and the local co-moving frame (Fig. 3) can be found as

$$\alpha = \cos^{-1}(l) \tag{56}$$

The deposition condition of the ellipsoidal fiber is transformed into the computation of its center of mass's vertical distance from the boundary surface. The deposition condition

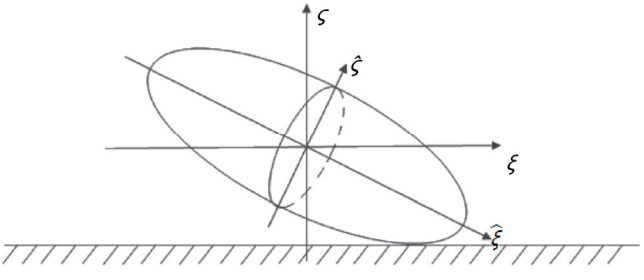

Fig. 3 Schematics of fiber deposition on a smooth surface (Tian et al., 2012; reproduced with permission © Elsevier Ltd. 2011).

is related to its orientation identified by the angle α in the local co-moving frame. The possible deposition point of the ellipsoid can be identified by (Fan and Ahmadi, 1995a):

$$\xi = \sqrt{\frac{(b^2-a^2)^2\left[\left(\frac{\cos\alpha}{a}\right)^2+\left(\frac{\sin\alpha}{b}\right)^2\right]\sin^2\alpha\cos^2\alpha}{\left\{1+a^2b^2\left[\left(\frac{1}{a^2}\right)-\left(\frac{1}{b^2}\right)\right]^2\sin^2\alpha\cos^2\alpha\right\}}} \tag{57}$$

and

$$\varsigma = \frac{-\xi\left(\frac{1}{a^2}-\frac{1}{b^2}\right)\sin\alpha\cos\alpha-\sqrt{\left(\frac{\cos\alpha}{a}\right)^2+\left(\frac{\sin\alpha}{b}\right)^2-\left(\frac{\xi}{ab}\right)^2}}{\left(\frac{\cos\alpha}{a}\right)^2+\left(\frac{\sin\alpha}{b}\right)^2} \tag{58}$$

A positive value of ς indicates no contact between the ellipsoidal fiber and the wall, while a negative value indicates that the fiber touches the wall boundary and is deposited.

3 Simplified Eulerian–Lagrangian (E–L) approach

When macroscale translational characteristics of fiber particles are of interest, while information on the orientation of each elongated particle is not needed, a simplified Eulerian–Lagrangian (E–L) approach can be employed. Here, the governing equation consists of only Eq. (12), while the angular momentum equations (Eqs. (13)–(15)) are neglected. The non-spherical particle dynamics is incorporated in the computational model with the use of a hydrodynamic shape factor C_D. The shape factor is evaluated using either an empirical correlation fitted to the particle free-fall measurements in viscous fluids (Lasso and Weidman, 1986; Haider and Levenspiel, 1989; Tran-Cong et al., 2004) or from theoretical derivations (Stöber, 1972).

3.1 Hydrodynamic drag

Hydrodynamic drag is an important force controlling the fate of a suspended particle. Tian et al. (2016) utilized the dynamic shape factor method to investigate the transport and deposition of welding fume agglomerates in the human nasal airway. Accordingly, the hydrodynamic drag is given as

$$F_D = \frac{1}{2}C_D\rho U^2 A \tag{59}$$

Here ρ is the fluid density, U is the slip velocity, and A is the projected area of the particle in the direction of the moving fluid. In their work, the dynamic shape factor C_D was from Tran-Cong et al. (2004) and in the form of

$$C_D = \frac{24}{Re}\frac{d_A}{d_n}\left[1+\frac{0.15}{\sqrt{c}}\left(\frac{d_A}{d_n}Re\right)^{0.687}\right] + \frac{0.42\left(\frac{d_A}{d_n}\right)^2}{\sqrt{c}\left[1+4.25\times10^4\left(\frac{d_A}{d_n}Re\right)^{-1.16}\right]} \tag{60}$$

where d_A is the surface equivalent sphere diameter, d_n is the volume equivalent sphere diameter, and c is the surface sphericity given by $\pi d_A/P_p$, in which P_p is the projected perimeter of the particle in its direction of motion, and Re is the particle Reynolds number given as

$$Re = \frac{\rho^p d_n U}{\mu} \tag{61}$$

where ρ^p is the particle density.

Alternatively, the Stokes hydrodynamic drag of a non-spherical particle is expressed as

$$F_D = 3\pi\mu U d_V K \tag{62}$$

where d_V is the volume-equivalent diameter, and K is a correction factor or the "dynamic shape factor". As discussed earlier, K can be obtained either experimentally (as C_D), or be derived theoretically. For elongated ellipsoid of revolution, K is given as (Stöber, 1972):

$$K_\perp = \frac{8(\beta^2-1)\beta^{-1/3}}{3\{[(2\beta^2-3)\ln(\beta+\sqrt{\beta^2-1})/\sqrt{\beta^2-1}]+\beta\}} \tag{63}$$

and

$$K_\parallel = \frac{4(\beta^2-1)\beta^{-1/3}}{3\{[(2\beta^2-1)\ln(\beta+\sqrt{\beta^2-1})/\sqrt{\beta^2-1}]-\beta\}} \tag{64}$$

where the subscript $\perp$ and $\parallel$ imply the dynamic shape factor measured in the lateral and principal directions, respectively. For orientation independent macroscale fiber distributions (or randomly oriented fibers), the overall dynamic shape factor K_r is given as (Happel and Brenner, 1973):

$$\frac{1}{K_r} = \frac{1}{3K_\parallel}+\frac{2}{3K_\perp} \tag{65}$$

3.2 Aerodynamic diameter

Assuming randomized orientation, the exact orientation of each individual fiber does not need to be resolved. The macroscale fiber dynamics can be characterized by the equivalent aerodynamic diameter to that of a sphere with the same settling velocity in a quiescent fluid. As a result, simplified Eulerian–Lagrangian (E–L) approach can be used.

According to Stöber (1972), the aerodynamic diameter d_a for an elongated ellipsoid fiber is given as

$$d_a = d_V \sqrt{\frac{\rho^p}{\rho_0 K_r}} \tag{66}$$

here ρ_0 is the unit density (1000 kg/m^3).

3.3 Stokes diameter

Similar to the fiber aerodynamic diameter, Shapiro and Goldenberg (1993) suggested using a relaxation time to characterize the motion of the ellipsoidal particle. Assuming that the fiber orientation is isotropic and using the averaged dyadic mobility (inverse of the translation dyadic), they suggested a Stokes diameter for the fiber. That is

$$d_{\text{Stokes\_Shapiro}} = 2a \sqrt{\frac{\beta \ln(\beta + \sqrt{\beta^2 - 1})}{\sqrt{\beta^2 - 1}}} \tag{67}$$

Instead of assuming the mobility dyadic, Fan and Ahmadi (1995a) used the orientation averaged translation dyadic. Accordingly, the equivalent Stokes diameter is given as

$$d_{\text{Stokes\_Fan}} = 6a \sqrt{\frac{2\beta}{K_{\hat{x}\hat{x}} + K_{\hat{y}\hat{y}} + K_{\hat{z}\hat{z}}}} \tag{68}$$

3.4 Shear-induced lift and Brownian diffusion force

Assuming a randomized distribution of fiber orientation in the simplified Eulerian–Lagrangian (E–L) approach, shear-induced lift and Brownian diffusion force were frequently calculated by using the formulas of volume-equivalent spherical particles in literature. Using the fiber mobility equivalent sphere, Tian et al. (2017) studied the fiber dispersion in inertial and high Knudsen number flows. Based on their study, an aerodynamic (or Stokes diameter) for the inertia flow and a surface equivalent diameter (or projected surface equivalent) diameter for the high Knudsen number flow should be used to characterize the fiber motion, respectively.

4 Fluid flow dynamics

The continuity and the Navier–Stokes equations for a viscous incompressible fluid are

$$\nabla \cdot \boldsymbol{u} = 0 \tag{69}$$

$$\frac{\partial \boldsymbol{u}}{\partial t} + \boldsymbol{u} \cdot \nabla \boldsymbol{u} = -\frac{1}{\rho} \nabla p + \nu \nabla^2 \boldsymbol{u} \tag{70}$$

where p is the fluid pressure. The solution of the fluid flow in terms of the velocity field is fed back into the fiber equations of motion that are given by Eqs. (12)–(15), for evaluating the fiber transport and dispersion.

Numerical solution to Eq. (70) for laminar flow is straightforward; however, for the turbulent flow regime, additional efforts are needed. Currently, there are three general approaches for simulating turbulent fluid flows. These are, the Reynolds-averaged Navier–Stokes (RANS) model method, direct numerical simulation (DNS), and large eddy simulation (LES). While DNS provides the most accurate capability for reproducing the features of turbulence up to the smallest eddies (Kolmogorov scale), the computational expenses associated with the current algorithm and need for excessive computing resources make it inapplicable to large Reynolds number flows or complex geometry applications. In the LES approach, the large eddies are directly simulated, while eddies smaller than the grid scales are modeled. LES is expected to provide a better representation of turbulence features beyond the filtered scales; however, the needed computational resources are still extensive. While the limitations of DNS and LES stated here make them impractical for applications to complex regions of industrial interest at the present time, these approaches have great potential with advances in the development of efficient algorithms and/or availability of ever-increasing computing resources. For current industrial applications of flows with large *Re* in complex passages, the RANS remains as the most commonly used approach. Details of turbulent flow simulation can be found in the work of Hinze (1975), Launder et al. (1975), Moser et al. (1999), Moin and Mahesh (1998), Hughes et al. (2001), Wilcox (2006), and among others.

5 Applications of fiber transport and deposition in human respiratory airways

5.1 Applications in human nasal cavities

Using the Eulerian–Lagrangian (E–L) approach and accounting for the hydrodynamic drag and torque, Dastan et al. (2014) computationally investigated the total and regional fiber deposition in human nasal cavities. Fibers with diameters of 2–30 μm, breathing rates of 2.5–10 L/min under laminar flow conditions were considered. Simulation results of the total deposition fraction of inhaled fibers in three different nasal cavities are summarized in Fig. 4.

Figure 4(a) shows that the total deposition increases with both the fiber diameter and aspect ratio, although some variations are observed between different nasal cavities. To formulate an equivalent diameter for collapsing the fiber deposition data into a narrow curve that can be compared with those of the spherical particles, Dastan et al. (2014) investigated a series of expressions and identified the equivalent aerodynamic diameter by combining Eqs. (66)

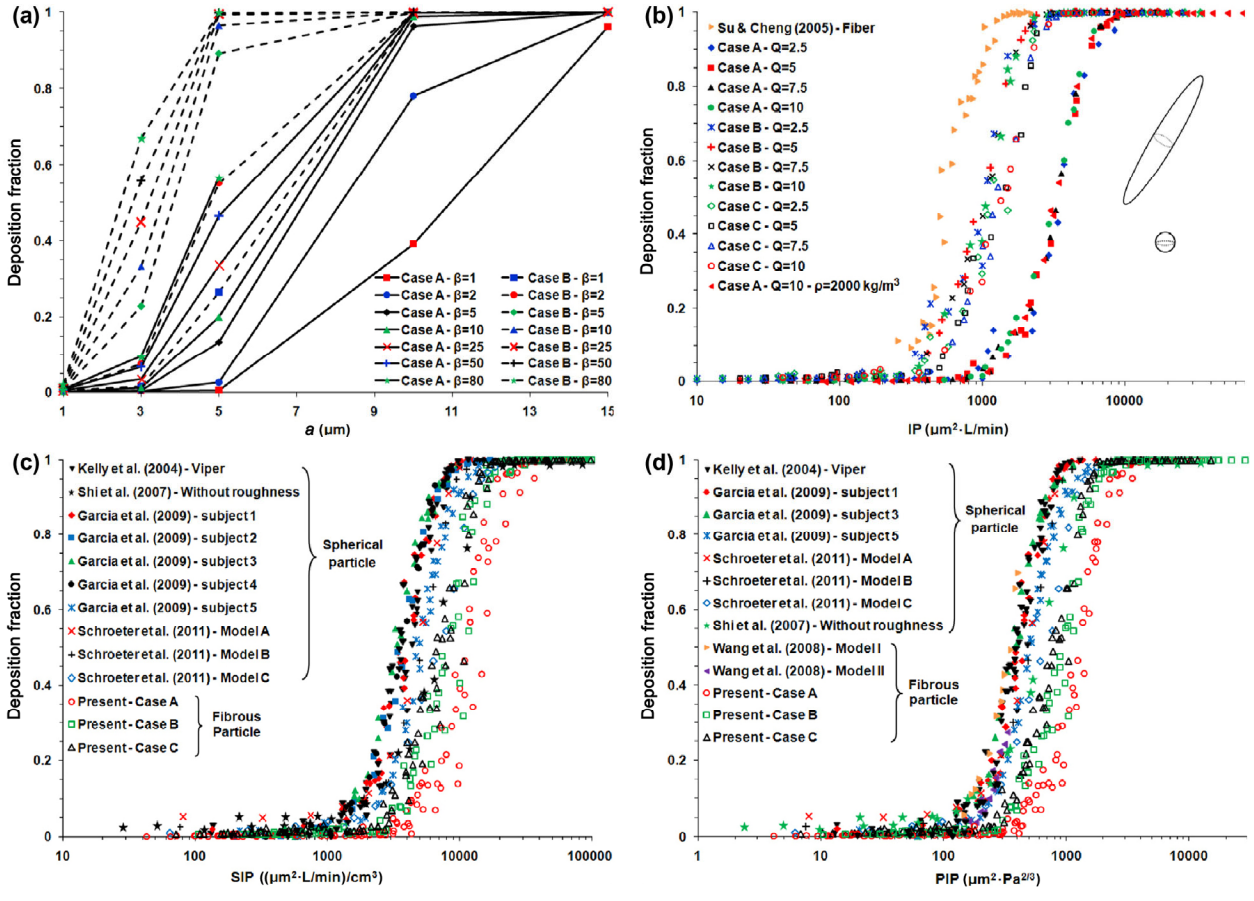

Fig. 4 (a) Fiber total deposition fraction against fiber semi-minor axis in two human nasal cavities at breathing rate Q = 7.5 L/min; (b) deposition fraction of unit density fibrous particles of diameter 2–30 μm and aspect ratio β from 1 to 80 versus impaction parameter (IP); (c) comparison of total fiber deposition fraction versus Stokes-based impaction parameter (SIP) with the spherical deposition fraction of earlier work (2 μm < d < 30 μm, 1 < β < 80); (d) comparison of total fiber deposition fraction versus pressure-based impaction parameter (PIP) with the spherical deposition fraction of earlier work (2 μm < d < 30 μm, 1 < β < 80) (Dastan et al., 2014; reproduced with permission © Elsevier Ltd. 2013).

and (68). That is, they replace d_V in Eq. (66) by $d_{\text{Stokes\_Fan}}$ (Eq. (68)), and set K_r = 1. Using the new aerodynamic diameter in the impaction parameter IP defined as, $d_{eq}^2 Q$, Dastan et al. (2014) compared the predicted deposition fraction of unit density fiber particles with the experimental measurement of Su and Cheng (2005) (Fig. 4(b)). They drew several conclusions: (1) impaction factor (IP) based on the proposed equivalent aerodynamic diameter was able to characterize the fiber deposition fraction in each nasal cavity by collapsing the deposition data into a narrow curve; (2) intersubject variability markedly affected fiber deposition fraction, and higher pressure drop in the nasal cavity led to an increased deposition of fiber particles; (3) simulation results were lower than the experimental measurement of Su and Cheng (2005).

To eliminate intersubject variability, two pressure-based impaction parameters SIP and PIP were proposed and tested for characterizing fiber deposition data across all subjects (Figs. 4(c) and 4(d)). The pressure-based impaction parameter (PIP) was derived by Garcia et al. (2009) as $d_{eq}^2 \Delta p^{2/3}$, while the Stokes-based impaction parameter was proposed by Dastan et al. (2014) as $d_{eq}^2 Q/d_c^3$. Here d_c is the characteristic diameter of the nasal passage defined as $(0.0181 L_{\text{nose}}/R_{\text{nose}})^{4/19}$, where L_{nose} is the linear distance from nostril to the end of the septum, and R_{nose} is the nasal cavity resistance defined as $\Delta p/Q^{1.75}$.

As shown in Figs. 4(c) and 4(d), both formulation of the pressure-based impaction parameters was able to collapse the deposition data (both ellipsoidal fibers and spherical particles) into a narrow band; thus, partially eliminated intersubject variability across different testing cases. Figures 4(c) and 4(d) show that for the same values of impaction parameters (SIP and PIP), the simulated fiber deposition fractions were significantly lower than the measured deposition fractions of the spherical particles.

Extending the work of Dastan et al. (2014), Tavakol et al. (2017) investigated the ellipsoidal fiber transport and deposition under turbulent flow regime (with Q > 12 L/min)

in a single nasal cavity (Cast B). In addition to the hydrodynamic drag and torque, the turbulent dispersion effects were accounted for in Eqs. (12)–(15). For fibers of diameter 2–20 μm, and aspect ratio from 2 to 80, the findings of Tavakol et al. (2017) are reproduced in Fig. 5. Here different stochastic models for generating turbulence fluctuations were used.

Based on the results presented in Fig. 5, the following important observations were made:

1) The *DRW* (discrete random walk) model of ANSYS-FLUENT overestimated the fiber deposition fraction for IP < 1000 due to the over-estimation of the normal near-wall turbulence fluctuations (Fig. 5(a)). A continuous random walk (CRW) model with modified near-wall turbulence normal RMS fluctuation was implemented using ANSYS-FLUENT-UDF (user-defined function), which produced more reasonable deposition rates (Fig. 5(a)).

2) The effect of turbulence dispersion was demonstrated in Fig. 5(b) by comparing the deposition data to those without accounting for the turbulence fluctuations; the study revealed that the influence of turbulent dispersion on particle transport and deposition was significant for 100 < IP < 2000, while for IP > 2000, turbulence effect was negligible.

3) Turbulence rotational diffusion did not affect the fiber particle deposition rate (Fig. 5(c)).

4) The equivalent Stokes diameter of Eq. (68) could be used to characterize the fiber transport and deposition rate (Fig. 5(d)).

Using the simplified Eulerian–Lagrangian (E–L) approach, Inthavong et al. (2008) and Shanley et al. (2018), respectively, investigated the inertial fiber deposition in human nasal cavities. Inthavong et al. (2008) used the fiber aerodynamic diameter defined by Eq. (66), and Shanley et al. (2018) employed an empirical equation suggested by Wang et al. (2008). The simulation results of these studies are presented in Fig. 6. It is seen that both studies obtained a similar deposition profile. Figure 6(a) shows that fiber simulation results were slightly higher than the experimental measurement of Su and Cheng (2005), while lower than experimental data for spherical particles (Pattle, 1961; Cheng et al., 2001; Kelly et al., 2004). Similar trend was seen in the simulation results of Shanley et al. (2018). It should be noted that the

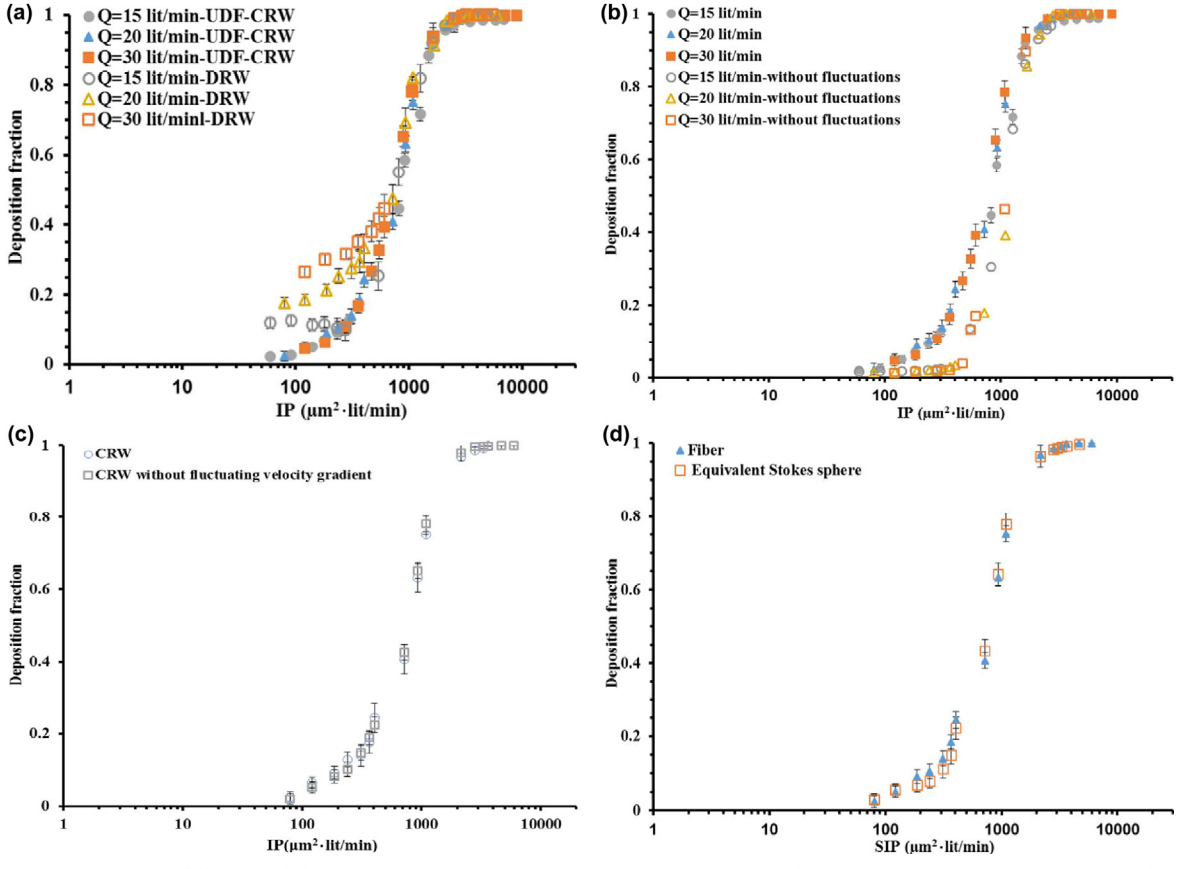

Fig. 5 (a) Comparison of fiber total deposition fraction against impaction parameter IP by using ANSYS-FLUENT DRW and modified CRW mode through ANSYS-FLUENT-UDF; (b) comparison of fiber total deposition fraction against impaction parameter IP with and without turbulence fluctuations; (c) comparison of fiber total deposition fraction against impaction parameter IP with and without turbulence rotational diffusion; (d) comparison of the total deposition fraction of fibers and equivalent Stokes spheres (Eq. (68)) versus the impaction parameter IP (Tavakol et al., 2017; reproduced with permission © Elsevier Ltd. 2017).

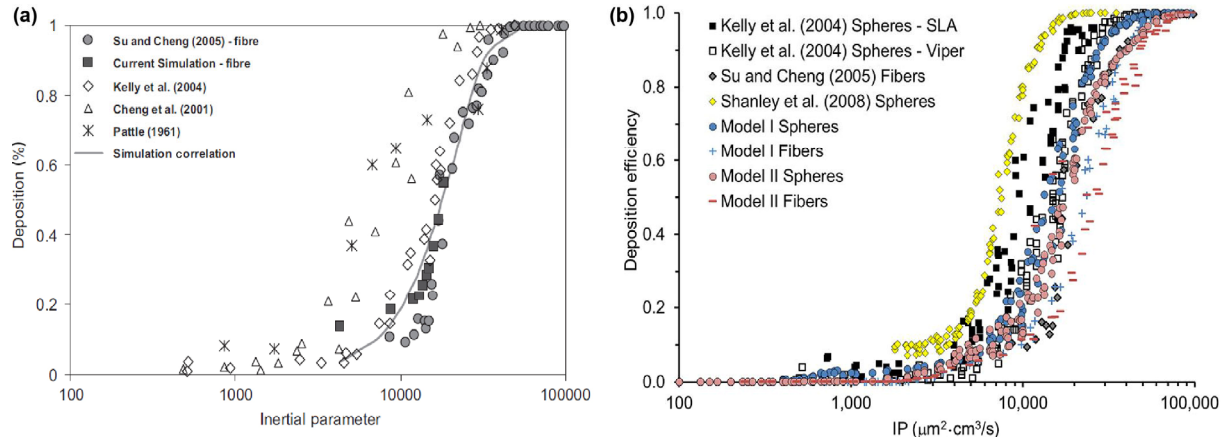

Fig. 6 (a) Fiber total deposition against inertial parameter (the same as impaction parameter IP) in human nasal cavities at Q = 7.5 L/min (Inthavong et al., 2008; reproduced with permission © Elsevier Ltd. 2007). (b) Fiber deposition efficiency versus impaction parameter (IP) (Shanley et al., 2018; reproduced with permission © Taylor & Francis 2018).

inertial parameter and impaction parameters (IP) in Figs. 6(a) and 6(b) have the same formulation.

In summary, the presented survey of existing literature showed that the majority of the earlier studies were on inertial fibers with the micrometer diameters. For this size range, the deposition rate is a function of the impaction parameter (IP). In the inertial range, fiber deposition increases with both length and diameter of fibers, as well as the IP. Simulated fiber deposition efficiency was also lower than the experimental measurement of spherical particles. This is attributed to the phenomenon that elongated fibers stay parallel to the wall in shear flows. The scatter in the data could be due to the surface roughness in the experiment, and intersubject variabilities. Turbulence fluctuations induce additional fiber deposition mainly in IP range of 100–2000 (μm²·L/min). Fiber deposition could be reasonably approximated with the equivalent Stokes or aerodynamics diameters.

5.2 Applications in human tracheobronchial airways

Using the Eulerian–Lagrangian (E–L) approach and accounting for the hydrodynamic drag, torque, gravitational, and lift forces, Tian and Ahmadi (2013) computationally investigated the fiber transport and deposition in human upper tracheobronchial airways containing trachea and the first three bifurcations. Fibers with diameters of 1, 2, and 3.66 μm, aspect ratios from 2 to 60 at breathing rates of 15, 40, and 60 L/min were studied. Due to laryngeal induced irregularity, airflow in the first three lung bifurcation was treated as being in the turbulent regime. The simulation study revealed fiber's rotational behavior along the trachea and in the bronchus (Fig. 7). In particular, it was shown that slender fibers tend to align with the main flow direction in the airway with occasional rapid rotation in the shear flow. The fiber rotation frequency was highly dependent on the fiber length (aspect ratio), and longer fibers had lower rotation frequency. Turbulence fluctuations tended to enhance the rotation of shorter fibers (Fig. 7(a)) but had less effect on the longer ones (Figs. 7(b) and 7(c)).

Comparison of the predicted deposition efficiency, against the non-dimensional relaxation time (τ+) in the trachea and first bifurcation, with the experimental measurement of Zhou et al. (2007) showed reasonable agreement (Fig. 8).

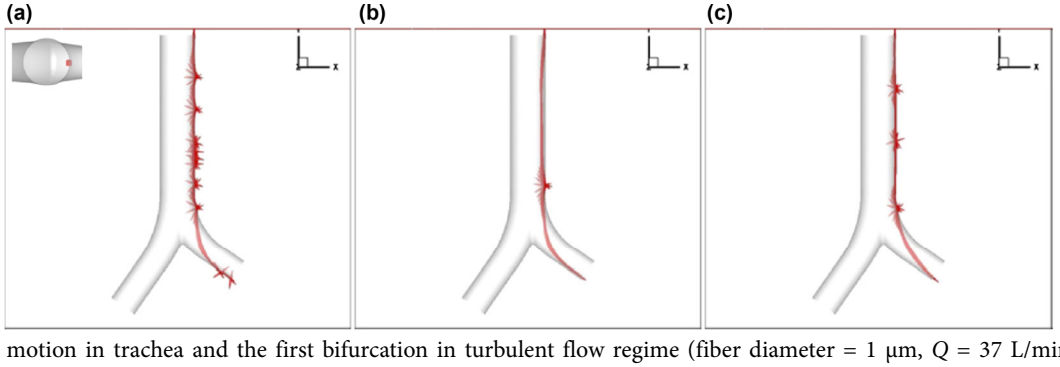

Fig. 7 Fiber motion in trachea and the first bifurcation in turbulent flow regime (fiber diameter = 1 μm, Q = 37 L/min): (a) β = 4; (b) β = 12; (c) β = 50 (Tian and Ahmadi, 2013; reproduced with permission © Elsevier Ltd. 2013).

The relaxation time, $\tau+$, for spherical particles is well defined. For elongated fibers, however, an equivalent formulation, similar to the methodology of the equivalent Stokes number taking account of the shape effect, was suggested (Tian and Ahmadi, 2013). Within a wide scattered data spread of both the experimental measurements and the computational results, turbulence shear velocity was found to be closely related to the fiber deposition rate. In the inertial range, fiber deposition was found to increase as the diameter, length, and $\tau+$ increased. Similar deposition trends were found in the 2nd and 3rd bifurcations.

The study also evaluated the fiber deposition characterization by using the equivalent Stokes spheres of Eq. (68), and good agreement was obtained (Fig. 9). On the contrary, using an equivalent volume sphere to approximate the fiber deposition found large discrepancies for fibers of diameters 2, 3.66, and 8 μm, but acceptable results for fibers of diameter 16 μm. Using the same Eulerian–Lagrangian (E–L) approach accounting for the hydrodynamic drag, torque, gravitational, and lift forces, Feng and Kleinstreuer (2013) performed fiber transport and deposition study in a 4-generation lung airway model including the oral cavity (Fig. 10(a)). For a fixed volume of ellipsoidal fibers, the total deposition efficiency was found to decrease with the aspect ratio, but the deposition efficiency rate increased with the breathing rate (Fig. 10(a)). By using the equivalent volume and equivalent Stokes diameters, the study compared the local fiber deposition in the oral cavity up to G5 of the tracheobronchial tree (Fig. 10(b)). Major findings were:

1) Equivalent volume diameter tends to overestimate the fiber deposition in the oral cavity, oropharynx, and larynx, while using the Stokes diameters led to reasonable predications.

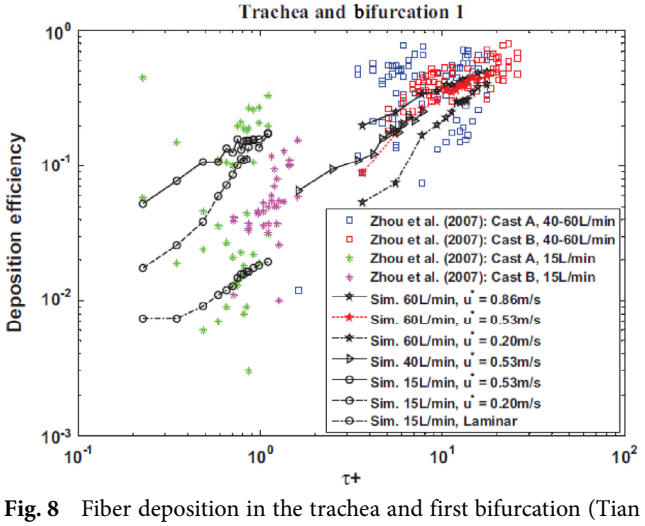

Fig. 8 Fiber deposition in the trachea and first bifurcation (Tian and Ahmadi, 2013; reproduced with permission © Elsevier Ltd. 2013).

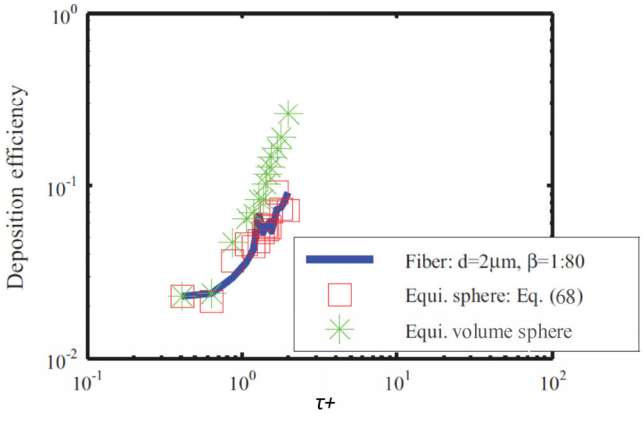

Fig. 9 Fiber motion in trachea and the first bifurcation in turbulent flow regime (fiber diameter = 1 μm, Q = 37 L/min): (a) β = 4; (b) β = 12; (c) β = 50 (Tian and Ahmadi, 2013; reproduced with permission © Elsevier Ltd. 2013).

2) Minor discrepancies were observed between the simulation results by using the E–L approach and equivalent diameters in G1 to G5 of the tracheobronchial tree, and the use of the equivalent Stokes diameters was not advantageous compared to the equivalent volume sphere in these regions.

Tian and Ahmadi (2016a, 2016b) performed a series of numerical simulations on nanofiber transport and deposition in the trachea and the first bifurcation. The airway geometry used was the same as that in the prior studies on micron fibers (Tian and Ahmaid, 2013). In addition to the hydrodynamic drag and torque, Brownian diffusion was also accounted for in the governing equations. In contrast to the micron fibers, for fixed diameter, the deposition efficiency of nanofibers decreased as the aspect ratio increased (Figs. 11(a)–11(c)). This finding points to the potential that very long nanofibers could penetrate deeper into the lung. Other significant findings were:

1) The Brownian diffusion dominated motions of the sub-micron fibers (nanofibers).

2) Brownian excitation enhanced the random rotation of shorter fibers while suppressed the rotation of longer ones.

3) Very thin and short nanofibers did not exhibit alignment with the main flow direction in airway passages, while very thin and long fibers tended to maintain their preferred alignment with the flow.

4) Deposition data correlated to the Peclet number in the submicron regime (Fig. 12). Equation (25) in Figs. 11 and 12 is the predicted fiber deposition efficiency in the trachea and the first bifurcation was compared with the empirical equation developed by Tian and Ahmadi (2016b).

Parameter S in Fig. 12 is the fiber particle-to-fluid density ratio (Tian and Ahmadi, 2016b).

Tian and Ahmadi (2016a) investigated the rotational contribution of Brownian excitation to the motion of

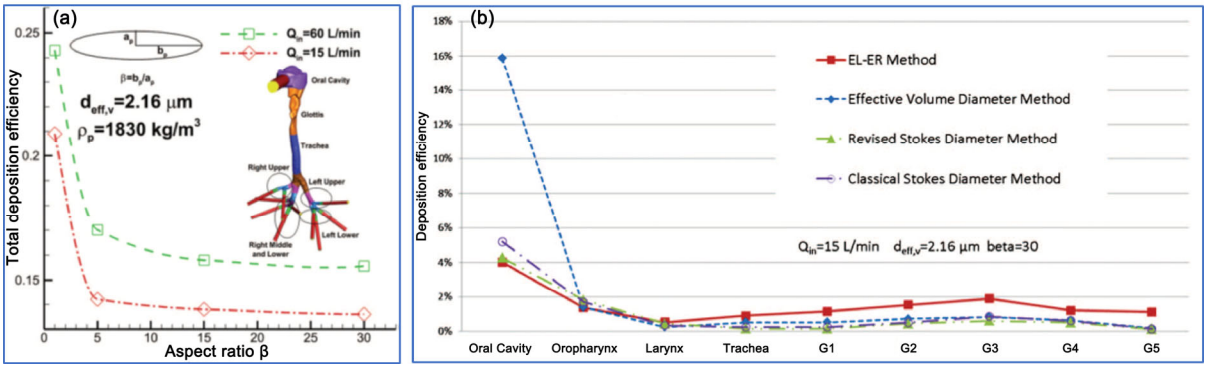

Fig. 10 (a) Fiber total deposition efficiency against aspect ratio in human oral and upper tracheobronchial airway branches (fiber volume equivalent diameter = 2.16 μm); (b) local deposition efficiency prediction by using Eulerian–Lagrangian (E–L) approach and equivalent diameters (Feng and Kleinstreuer, 2013; reproduced with permission © AIP Publishing LLC. 2013).

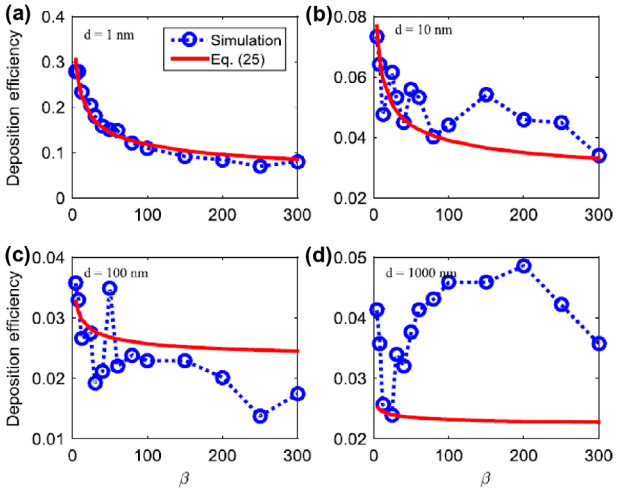

Fig. 11 Fiber deposition efficiency versus the aspect ratio in the trachea and the first bifurcation at Q = 37 L/min (Tian and Ahmadi, 2016b; reproduced with permission © Elsevier Ltd. 2015).

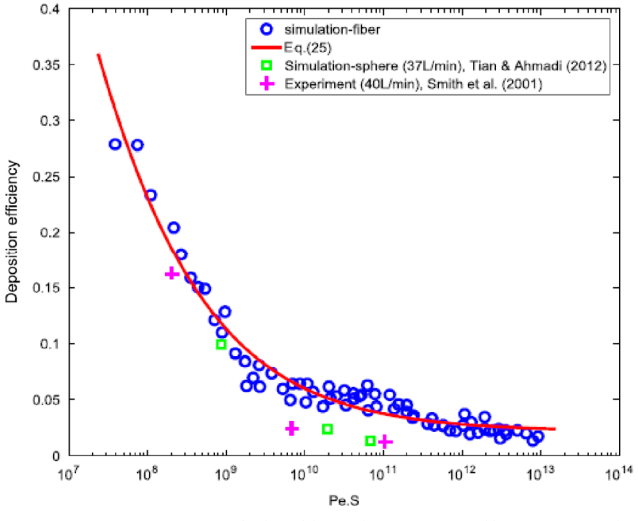

Fig. 12 Comparison of the fiber deposition efficiency in the trachea and the first bifurcation (Tian and Ahmadi, 2016b; reproduced with permission © Elsevier Ltd. 2015).

nanofibers in the human trachea and the first bronchi. They reported that the combination of turbulence dispersion and Brownian diffusion significantly enhanced the fiber deposition rate, while turbulence or Brownian alone was not able to produce the same level of deposition (Fig. 13(b)). Furthermore, the effect of Brownian rotational excitation is negligible whereas the translational Brownian excitation plays a major role in the fiber deposition processes.

6 Summary and future research need

This article reviewed the current state of computational modeling of micron and nano elongated particle dynamics and their application to fiber transport and deposition in human respiratory airways. Accordingly, the most versatile, efficient, and practical approach is the Eulerian–Lagrangian (E–L) simulation methodology. In this approach, the details of the translational and rotational motions of fibers, and their couplings are simulated. In particular, the influences of the rotation on the fiber macroscopic transport and deposition are evaluated. The methodology is flexible and can accommodate different flow models for the continuous phase, and at the same time, the model is robust in accounting for various particle–fluid interactions.

Of the reported applications on fiber deposition in the human nasal cavity, all earlier studies were focused on quantifying the total or regional deposition fractions and developing correlations to the equivalent diameter spheres. Currently, only inertial fiber particles (micron size range) were investigated, and the deposition fraction correlations to impaction parameters (IP) were evaluated. In the inertial range, it was found that the fiber deposition rate increases with both its length and diameter, as well as to appropriately formulated impaction parameters (IP). In particular, the equivalent Stokes number was able to characterize the deposition of fibers in the human nasal cavity reasonably well. While the intersubject variability brings additional

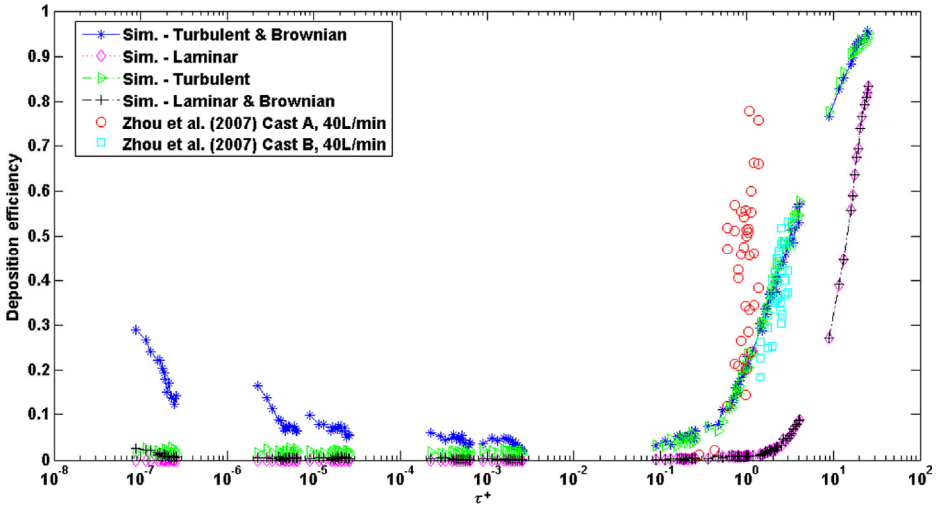

Fig. 13 Comparison of the fiber deposition efficiencies in the trachea and the first bifurcation (Tian and Ahmadi, 2016a; reproduced with permission © ASME 2016).

complexity to the problem, by proper selection of the impaction parameter (IP), the variability can be reduced but not eliminated.

Comparisons of the simulations results with the experimental data of both spherical and fiber particles showed good agreement on the deposition rate, however, not conclusive about the subtle differences between fibers and the spherical particles on the same benchmark parameters. For the same impaction parameters (SIP/PIP/IP), experimentally measured deposition rates of spherical particles were always higher than those of the fiber deposition rates. This was attributed to the phenomenon that elongated fibers stay parallel to the wall in shear flows. The surface roughness in experiment and intersubject variabilities may also play a role.

Contributions of turbulent dispersion to fiber deposition were also analyzed, and it was found that for the lower IP values ($100 < IP < 2000$), turbulent diffusion significantly enhances fiber deposition rate; however, for $IP > 2000$ the effect of turbulence on fiber deposition is negligible.

Although quantitative analysis of the fiber deposition rate in the human nasal cavity was performed, the detailed understanding of the fiber–fluid interactions and their influence on transport processes are yet to be provided. Currently, the role of the fiber rotation along its path in interpreting the fiber deposition data has not been fully elucidated. In this regard, detailed analysis of the fiber fully coupled translational and rotational motions will be of significant benefit.

Due to geometric complexity, simulations of the fiber transport and deposition in the human lung were performed only in the first few generations of the tracheobronchial tree. Nevertheless, these studies qualitatively identified that the very long and slender fibers could penetrate the upper airways into the deep lung and pose extreme health hazards. The deposition rate of the inhaled fibers in selected tracheobronchial airways was simulated, and the capability of using spherical equivalent diameters to characterize fiber deposition was also evaluated. These studies found that the fiber equivalent relaxation time and Stokes diameters were able to characterize fiber deposition reasonably well. However, the effect of using the equivalent volume diameter was not conclusive. While studies of Tian and Ahmadi (2013) noted the overprediction of fiber deposition efficiency in human upper tracheobronchial airways by using fiber equivalent volume diameters, the investigation of Feng and Kleinstreuer (2013) indicated reasonable fiber deposition prediction in G1 to G5 of the tracheobronchial tree beyond larynx.

In addition to the inertial fibers, the transport and deposition of nanofibers under high Knudsen number conditions in human tracheobronchial airways were studied. Instead of the equivalent Stokes diameters, the deposition results of the nanofibers correlated closely to the Peclet number. Tian et al. (2016, 2017) presented a detailed comparison of the various equivalent diameters in characterizing nanofiber dynamics. While they identified the surface dominated transport mechanisms as most pertinent to the high Knudsen number flows, the application of these findings to deposition in tracheobronchial airways has yet to be reported. Preliminary studies, however, suggest that the rotational diffusion due to turbulence fluctuations and Brownian excitation do not make a significant contribution to fiber deposition in human upper tracheobronchial airways. Similarly, systematic analysis of the fiber fully coupled translational and rotational motions are needed in human nasal cavities and in the lower airway passages to interpret role of the rotation in the fiber transport and deposition processes.

To fully understand the respiratory transport and deposition of airborne asbestos/man-made vitreous fibers (MMVFs)/carbon nanofiber/carbon nanotubes, and comprehend why such needle-like slender particles are so hazardous to human respiratory health, significant researches are still needed. In particular, providing full information on the role of the rotation, shape and particle-fluid interactions of non-spherical particles in comparison with the spherical particles is critical. In particular, future research in the following areas are needed:

- Fiber dynamics in the high Knudsen flow regimes. Most prior studies in human respiratory systems were on inertial fibers, and more studies investigating the transport behavior of the nanofibers are needed.
- Individual fiber dynamics to reveal the intrinsic relationship between the particle's unique elongated shape and the transport characteristics in human respiratory systems.
- A comprehensive investigation of suitable fiber equivalent diameters for characterizing fiber transport and deposition in human respiratory airways. While the particle flow regimes will be the critical factor, the regional airway geometries may also affect the selection of appropriate equivalent sphere parameter.
- Detailed information on the role of the fiber rotation, shape and particle–fluid interactions in order to gain more in-depth insight of elongated particle hazard to human respiratory health.
- Detailed analysis of the fiber deposition model and the effect of rotational interceptions on fiber deposition study in human respiratory airways.
- Complete respiratory airway modeling covering from the nasal and oral cavities, upper and lower tracheobronchial tree, and down to the deep lung passages and alveolar ducts.
- Providing more comprehensive experimental data for fiber transport and deposition in human and animal respiratory airways.
- Detailed analysis of fiber transport and deposition under transient breathing conditions.
- Including the effects of non-creeping flow condition on the simulation of fiber transport and deposition.

Acknowledgements

The financial supports provided by the Australian Research Council (Grant No. DE 180101138) and the National Institute for Occupational Safety and Health (NIOSH Grant No. R01 OH003900) are gratefully acknowledged.

References

Asgharian, B., Ahmadi, G. 1998. Effect of fiber geometry on deposition in small airways of the lung. *Aerosol Sci Tech*, 29: 459–474.

Batchelor, G. K. 1970. Slender-body theory for particles of arbitrary cross-section in Stokes flow. *J Fluid Mech*, 44: 419–440.

Brenner, H. 1963. The Stokes resistance of an arbitrary particle. *Chem Eng Sci*, 18: 1–25.

Brown, R. C. 1994. Man-made mineral fibres: Hazard, risk and regulation. *Indoor Environ*, 3: 237–247.

Burgers, J. M. 1938. Second report on viscosity and plasticity. Prepared by the Committee for the Study of Viscosity of the Academy of Sciences at Amsterdam. *Kon Ned Akad Wet Verhand*, 16: 1–287.

Cavallo, D., Campopiano, A., Cardinali, G., Casciardi, S., De Simone, P., Kovacs, D., Perniconi, B., Spagnoli, G., Ursini, C. L., Fanizza, C. 2004. Cytotoxic and oxidative effects induced by man-made vitreous fibers (MMVFs) in a human mesothelial cell line. *Toxicology*, 201: 219–229.

Chandrasekhar, S. 1943. Stochastic problems in physics and astronomy. *Rev Mod Phys*, 15: 1–89.

Cheng, Y. S., Holmes, T. D., Gao, J., Guilmette, R. A., Li, S., Surakitbanharn, Y., Rowlings, C. 2001. Characterization of nasal spray pumps and deposition pattern in a replica of the human nasal airway. *J Aerosol Med*, 14: 267–280.

Cheng, Y. S., Yeh, H. C., Allen, M. D. 1988. Dynamic shape factor of a plate-like particle. *Aerosol Sci Tech*, 8: 109–123.

Chhabra, R. P., Singh, T., Nandrajog, S. 1995. Drag on chains and agglomerates of spheres in viscous Newtonian and power law fluids. *Can J Chem Eng*, 73: 566–571.

Cichocki, B., Hinsen, K. 1995. Stokes drag on conglomerates of spheres. *Phys Fluids*, 7: 285–291.

Cui, Y., Ravnik, J., Hriberšek, M., Steinmann, P. 2018. A novel model for the lift force acting on a prolate spheroidal particle in an arbitrary non-uniform flow. Part I. Lift force due to the streamwise flow shear. *Int J Multiphase Flow*, 104: 103–112.

Cunningham, E. 1910. On the velocity of steady fall of spherical particles through fluid medium. *Proc R Soc Lond A*, 83: 357–365.

Dahneke, B. E. 1973. Slip correction factors for nonspherical bodies—III the form of the general law. *J Aerosol Sci*, 4: 163–170.

Dastan, A., Abouali, O., Ahmadi, G. 2014. CFD simulation of total and regional fiber deposition in human nasal cavities. *J Aerosol Sci*, 69: 132–149.

Einstein, A. 1905. On the motion of small particles suspended in a stationary liquid, as required by the molecular kinetic theory of heat. *Annalen der Physik*, 17: 549–560.

Eisner, A. D., Gallily, I. 1981. On the stochastic nature of the motion of nonspherical aerosol particles. *J Colloid Interface Sci*, 81: 214–233.

EPA. 2003. Report on the peer consultation workshop to discuss a proposed protocol to assess asbestos-related risk, final report. Office of Solid Waste and Emergency Response, Washington D.C.

Epstein, P. S. 1924. On the resistance experienced by spheres in their motion through gases. *Phys Rev*, 23: 710–733.

Fan, F. G., Ahmadi, G. 1995a. A sublayer model for wall deposition of ellipsoidal particles in turbulent streams. *J Aerosol Sci*, 26: 813–840.

Fan, F. G., Ahmadi, G. 1995b. Dispersion of ellipsoidal particles in an isotropic pseudo-turbulent flow field. *J Fluid Eng*, 117: 154–161.

Fan, F. G., Ahmadi, G. 2000. Wall deposition of small ellipsoids from turbulent air flows—a Brownian dynamics simulation. *J Aerosol Sci*, 31: 1205–1229.

Fan, F. G., Soltani, M., Ahmadi, G., Hart, S. C. 1997. Flow-induced resuspension of rigid-link fibers from surfaces. *Aerosol Sci Tech*, 27: 97–115.

Feng, Y., Kleinstreuer, C. 2013. Analysis of non-spherical particle transport in complex internal shear flows. *Phys Fluids*, 25: 091904.

Gallily, I., Cohen, A. H. 1979. On the orderly nature of the motion of nonspherical aerosol particles. II. Inertial collision between a spherical large droplet and an axially symmetrical elongated particle. *J Colloid Interf Sci*, 68: 338–356.

Gans, R. 1928. Zur Theorie der Brownschen Molekularbewegung. *Ann Phys*, 391: 628–656.

Garcia, G. J. M., Tewksbury, E. W., Wong, B. A., Kimbell, J. S. 2009. Interindividual variability in nasal filtration as a function of nasal cavity geometry. *J Aerosol Med Pulm D*, 22: 139–156.

Goldstein, H. 1980. *Classical Mechanics*, 2nd edn. Addison-Wesley.

Guo, X. H., Lin, J. Z., Nie, D. M. 2011. New formula for drag coefficient of cylindrical particles. *Particuology*, 9: 114–120.

Gupta, D., Peters, M. H. 1985. A Brownian dynamics simulation of aerosol deposition onto spherical collectors. *J Colloid Interf Sci*, 104: 375–389.

Haider, A., Levenspiel, O. 1989. Drag coefficient and terminal velocity of spherical and nonspherical particles. *Powder Technol*, 58: 63–70.

Happel, J., Brenner, H. 1973. *Low Reynolds Number Hydrodynamics*. Leyden: Noordhoff.

Harper, E. Y., Chang, I. D. 1968. Maximum dissipating resulting from lift in a slow viscous flow. *J Fluid Mech*, 33: 209–225.

Hesterberg, T. W., Anderson, R., Bernstein, D. M., Bunn, W. B., Chase, G. A., Jankousky, A. L., Marsh, G. M., McClellan, R. O. 2012. Product stewardship and science: Safe manufacture and use of fiber glass. *Regul Toxicol Pharm*, 62: 257–277.

Hinze, J. O. 1975. *Turbulence*, 2nd edn. New York: McGraw-Hill.

Hölzer, A., Sommerfeld, M. 2009. Lattice Boltzmann simulations to determine drag, lift and torque acting on non-spherical particles. *Comput Fluids*, 38: 572–589.

Horvath, H. 1974. The sedimentation behavior of non-spherical particles. *Staub Reinhalt Luft*, 34: 197–202.

Hughes, J. M., Jones, R. N., Glindmeyer, H. W., Hammad, Y. Y., Weill, H. 1993. Follow up study of workers exposed to man made mineral fibres. *Occup Environ Med*, 50: 658–667.

Hughes, P. C. 1986. *Spacecraft Attitude Dynamics*. New York: Wiley.

Hughes, T. J. R., Oberai, A. A. O., Mazzei, L. 2001. Large eddy simulation of turbulent channel flows by the variational multiscale method. *Phys Fluids*, 13: 1784–1799.

International Agency for Research on Cancer (IARC). 2002. IARC monographs on the evaluation of carcinogenic risks to humans. man-made vitreous fibres. IARC, Lyon, 81: 1–418.

Inthavong, K., Wen, J., Tian, Z. F., Tu, J. Y. 2008. Numerical study of fibre deposition in a human nasal cavity. *J Aerosol Sci*, 39: 253–265.

Invernizzi, N. 2011. Nanotechnology between the lab and the shop floor: What are the effects on labor? *J Nanopart Res*, 13: 2249–2268.

Jeffery, G. B. 1922. The motion of ellipsoidal particles immersed in a viscous fluid. *P Roy Soc A*, 102: 161–179.

Kelly, J. T., Asgharian, B. C., Kimbell, J. S., Wong, B. A. 2004. Particle deposition in human nasal airway replicas manufactured by different methods. Part I: inertial regime particles. *Aerosol Sci Tech*, 38: 1063–1071.

Kvasnak, W., Ahmadi, G. 1996. Deposition of ellipsoidal particles in turbulent duct flows. *Chem Eng Sci*, 51: 5137–5148.

Lam, C.-W., James, J. T., McClusjey, R., Hunter, R. L. 2004. Pulmonary toxicity of single-wall carbon nanotubes in mice 7 and 90 days after intratracheal instillation. *Toxical Sci*, 77: 126–134.

Lasso, I. A., Weidman, P. D. 1986. Stokes drag on hollow cylinders and conglomerates. *Phys Fluids*, 29: 3921–3934.

Launder, B. E., Reece, G. J., Rodi, W. 1975. Progress in the development of a Reynolds-stress turbulence closure. *J Fluid Mech*, 68: 537–566.

LeMasters, G. K., Lockey, J. E., Yiin, J. H., Hilbert, T. J., Levin, L. S., Rice, C. H. 2003. Mortality of workers occupationally exposed to refractory ceramic fibers. *J Occup Environ Med*, 45: 440–450.

Li, K., Ma, H. L. 2018. Deposition dynamics of rod-shaped colloids during transport in porous media under favorable conditions. *Langmuir*, 34: 2967–2980.

Lippmann, M. 1988. Asbestos exposure indices. *Environ Res*, 46: 86–106.

Lippmann, M. 2014. Toxicological and epidemiological studies on effects of airborne fibers: Coherence and public health implications. *Crit Rev Toxicol*, 44: 643–695.

Luo, S., Wang, J., Yu, S., Xia, G. D., Li, Z. G. 2018. Shear lift forces on nanocylinders in the free molecule regime. *J Fluid Mech*, 846: 392–410.

Ma-Hock, L., Treumann, S., Strauss, V., Brill, S., Luizi, F., Mertler, M., Wiench, K., Gamer, A. O., van Ravenzwaay, B., Landsiedel, R. 2009. Inhalation toxicity of multiwall carbon nanotubes in rats exposed for 3 months. *Toxicol Sci*, 112: 468–481.

Marsh, G. M., Buchanich, J. M., Youk, A. O. 2001. Historical cohort study of US man-made vitreous fiber production workers: VI. respiratory system cancer standardized mortality ratios adjusted for the confounding effect of cigarette smoking. *J Occup Environ Med*, 43: 803–808.

McNown, J. S., Malaika, J. 1950. Effects of particle shape on settling velocity at low Reynolds numbers. *Eos Trans AGU*, 31: 74–82.

Mercer, R. R., Hubbs, A. F., Scabilloni, J. F., Wang, L., Battelli, L. A., Friend, S., Castranova, V., Porter, D. W. 2011. Pulmonary fibrotic response to aspiration of multi-walled carbon nanotubes. *Part Fibre Toxicol*, 8: 21.

Mercer, R. R., Scabilloni, J., Wang, L., Kisin, E., Murray, A. R., Schwegler-Berry, D., Shvedova, A. A., Castranova, V. 2008. Alteration of deposition pattern and pulmonary response as a result of improved dispersion of aspirated single-walled carbon nanotubes in a mouse model. *Am J Physiol-Lung C*, 294: L87–L97.

Moin, P., Mahesh, K. 1998. DIRECT NUMERICAL SIMULATION: A tool In turbulence research. *Ann Rev Fluid Mech*, 30: 539–578.

Moser, R. D., Kim, J., Mansour, N. N. 1999. Direct numerical simulation of turbulent channel flow up to Re_τ=590. *Phys Fluids*, 11: 943–945.

Muller, J., Huaux, F., Moreau, N., Misson, P., Heilier, J. F., Delos, M., Arras, M., Fonseca, A., Nagy, J. B., Lison, D. 2005. Respiratory toxicity of multi-wall carbon nanotubes. *Toxicol Appl Pharmacoly*, 207: 221–231.

Murphy, F. A., Poland, C. A., Duffin, R., Al-Jamal, K. T., Ali-Boucetta, H., Nunes, A., Byrne, F., Prina-Mello, A., Volkov, Y., Li, S., et al. 2011. Length-dependent retention of carbon nanotubes in the pleural space of mice initiates sustained inflammation and progressive fibrosis on the parietal pleura. *Am J Pathol*, 178: 2587–2600.

Murray, A. R., Kisin, E. R., Tkach, A. V., Yanamala, N., Mercer, R., Young, S. H., Fadeel, B., Kagan, V. E., Shvedova, A. A. 2012. Factoring-in agglomeration of carbon nanotubes and nanofibers for better prediction of their toxicity versus asbestos. *Part Fibre Toxicol*, 9: 10.

Nielsen, G. D., Koponen, I. K. 2018. Insulation fiber deposition in the airways of men and rats. A review of experimental and computational studies. *Regul Toxicol Pharm*, 94: 252–270.

NIOSH. 1990. Comments of the National Institute for Occupational Safety and Health on the Occupational Safety and Health Administration's Notice of Proposed Rulemaking on Occupational Exposure to Asbestos, Tremolite, Anthophyllite, and Actinolite. OSHA Docket no. H-033d, April 9, 1990.

NIOSH. 2008. Strategic plan for NIOSH nanotechnology research and guidance: Filling the knowledge gaps. Available at https://stacks.cdc.gov/view/cdc/5481.

Njobuenwu, D. O., Fairweather, M. 2014. Effect of shape on inertial particle dynamics in a channel flow. *Flow Turbul Combust*, 92: 83–101.

Njobuenwu, D. O., Fairweather, M. 2015. Dynamics of single, non-spherical ellipsoidal particles in a turbulent channel flow. *Chem Eng Sci*, 123: 265–282.

Njobuenwu, D. O., Fairweather, M. 2017. Large eddy simulation of inertial fiber deposition mechanisms in a vertical downward turbulent channel flow. *AIChE J*, 63: 1451–1465.

Oberbeck, A. J. 1876. Ueber stationäre Flüssigkeitsbewegungen mit Berücksichtigung der inneren Reibung. *Journal Für Die Reine Und Angewandte Mathematik (Crelles Journal)*, 1876: 62–80.

Oseen, C. W. 1927. *Hydrodynamik*. Leipzig: Akademische Verlagsgesellshaf.

Ouchene, R., Khalij, M., Arcen, B., Tanière, A. 2016. A new set of correlations of drag, lift and torque coefficients for non-spherical particles and large Reynolds numbers. *Powder Technol*, 303: 33–43.

Ounis, H., Ahmadi, G., McLaughlin, J. B. 1991. Brownian diffusion of submicrometer particles in the viscous sublayer. *J Colloid Interf Sci*, 143: 266–277.

Pattle, R. E. 1961. The retention of gases and particles in the human nose. In: *Inhaled Particles and Vapors*. Davies, C. N. ed. Oxford, UK: Pergamon Press.

Poland, C. A., Duffin, R., Kinloch, I., Maynard, A., Wallace, W. A. H., Seaton, A., Stone, V., Brown, S., MacNee, W., Donaldson, K. 2008. Carbon nanotubes introduced into the abdominal cavity of mice show asbestos-like pathogenicity in a pilot study. *Nat Nanotech*, 3: 423–428.

Porter, D. W., Hubbs, A. F., Mercer, R. R., Wu, N., Wolfarth, M. G., Sriram, K., Leonard, S., Battelli, L., Schwegler-Berry, D., Friend, S. 2010. Mouse pulmonary dose- and time course-responses induced by exposure to multi-walled carbon nanotubes. *Toxicology*, 269: 136–147.

Pott, F., Ziem, U., Reiffer, F. J., Huth, F., Ernst, H., Mohr, U. 1987. Carcinogenicity studies on fibres, metal compounds, and some other dusts in rats. *Exp Pathol*, 32: 129–152.

Saffman, P. G. 1965. The lift on a small sphere in a slow shear flow. *J Fluid Mech*, 22: 385–400.

Schubauer-Berigan, M. K., Dahm, M. M., Yencken, M. S. 2011. Engineered carbonaceous nanomaterials manufacturers in the United States. *J Occup Environ Med*, 53: S62–S67.

Service, R. F. 1998. Nanotubes: The next asbestos? *Science*, 281: 941.

Shanley, K. T., Ahmadi, G., Hopke, P. K., Cheng, Y. S. 2018. Simulated airflow and rigid fiber behavior in a realistic nasal airway model. *Particul Sci Technol*, 36: 131–140.

Shanley, K. T., Zamankhan, P., Ahmadi, G., Hopke, P. K., Cheng, Y. S. 2008. Numerical simulations investigating the regional and overall deposition efficiency of the human nasal cavity. *Inhal Toxicol*, 20: 1093–1100.

Shapiro, M., Goldenberg, M. 1993. Deposition of glass fiber particles from turbulent air flow in a pipe. *J Aerosol Sci*, 24: 65–87.

Simonato, L., Fletcher, A. C., Cherrie, J. W., Andersen, A., Bertazzi, P., Charnay, N., Claude, J., Dodgson, J., Esteve, J., Frentzel-Beyme, R., et al. 1987. The international agency for research on cancer historical cohort study of MMMF production workers in seven European countries: Extension of the follow-up. *Ann Occup Hyg*, 31: 603–623.

Stöber, W. 1972. Dynamic shape factors of nonspherical aerosol particles. In: *Assessment of Airborne Particles*. Mercer, T., et al. Eds. Springfield, IL: Charles C. Thomas: 249–289.

Stokes, G. G. 1851. On the effect of internal friction of fluids on the motion of pendulums. *Trans Cam Phil Soc*, 9: 8–106.

Su, W. C., Cheng, Y.-S. 2005. Deposition of fiber in the human nasal airway. *Aerosol Sci Tech*, 39: 888–901.

Tavakol, M. M., Abouali, O., Yaghoubi, M., Ahmadi, G. 2015. Dispersion and deposition of ellipsoidal particles in a fully developed laminar pipe flow using non-creeping formulations for hydrodynamic forces and torques. *Int J Multiphase Flow*, 75: 54–67.

Tavakol, M. M., Ghahramani, E., Abouali, O., Yaghoubi, M., Ahmadi, G. 2017. Deposition fraction of ellipsoidal fibers in a model of human nasal cavity for laminar and turbulent flows. *J Aerosol Sci*, 113: 52–70.

Tian, L., Ahmadi, G. 2013. Fiber transport and deposition in human upper tracheobronchial airways. *J Aerosol Sci*, 60: 1–20.

Tian, L., Ahmadi, G. 2016a. On nano-ellipsoid transport and deposition in the lung first bifurcation-effect of slip correction. *J Fluid Eng*, 138: 101101.

Tian, L., Ahmadi, G. 2016b. Transport and deposition of nano-fibers in human upper tracheobronchial airways. *J Aerosol Sci*, 91: 22–32.

Tian, L., Ahmadi, G., Tu, J. 2016. Brownian diffusion of fibers. *Aerosol Sci Tech*, 50: 474–486.

Tian, L., Ahmadi, G., Tu, J. Y. 2017. Mobility of nanofiber, nanorod, and straight-chain nanoparticles in gases. *Aerosol Sci Tech*, 51: 587–601.

Tian, L., Ahmadi, G., Wang, Z. C., Hopke, P. K. 2012. Transport and deposition of ellipsoidal fibers in low Reynolds number flows. *J Aerosol Sci*, 45: 1–18.

Tian, L., Inthavong, K., Lidén, G., Shang, Y. D., Tu, J. Y. 2016. Transport and deposition of welding fume agglomerates in a realistic human nasal airway. *Ann Occup Hyg*, 60: 731–747.

Tran-Cong, S., Gay, M., Michaelides, E. E. 2004. Drag coefficients of irregularly shaped particles. *Powder Technol*, 139: 21–32.

Uhlenbeck, G. E., Ornstein, L. S. 1930. On the theory of the Brownian motion. *Phys Rev*, 36: 823–841.

Wagner, C. J. 1986. Mesothelioma and mineral fibers, accomplishments in cancer research 1985 prize year. General Motors Cancer Research Foundation: 60–72.

Wang, Z. C., Hopke, P. K., Ahmadi, G., Cheng, Y.-S., Baron, P. A. 2008. Fibrous particle deposition in human nasal passage: The influence of particle length, flow rate, and geometry of nasal airway. *J Aerosol Sci*, 39: 1040–1054.

Wilcox, D. C. 2006. *Turbulence Modeling for CFD*, 3rd edn. DCW Industries.

Yin, C., Rosendahl, L., Kær, S. K., Condra, T. J. 2004. Use of numerical modeling in design for co-firing biomass in wall-fired burners. *Chem Eng Sci*, 59: 3281–3292.

Zastawny, M., Mallouppas, G., Zhao, F., van Wachem, B. 2012. Derivation of drag and lift force and torque coefficients for non-spherical particles in flows. *Int J Multiphase Flow*, 39: 227–239.

Zhang, H. F., Ahmadi, G., Fan, F. G., McLaughlin, J. B. 2001. Ellipsoidal particles transport and deposition in turbulent channel flows. *Int J Multiphase Flow*, 27: 971–1009.

Zhou, Y., Su, W.-C., Cheng, Y. S. 2007. Fiber deposition in the tracheabronhical region: Experimental measurements. *Inhal Toxicol*, 19: 1071–1078.